*Meteoritics & Planetary Science* 37, 1299–1321 (2002)
Available online at http://www.uark.edu/meteor

# Chondrule thermal history from unequilibrated H chondrites: A transmission and analytical electron microscopy study

C. FERRARIS[1]*, L. FOLCO[2] AND M. MELLINI[1]

[1]Dipartimento di Scienze della Terra, Università di Siena, Via Laterina 8, I-53100 Siena, Italy
[2]Museo Nazionale dell'Antartide, Università di Siena, Via Laterina 8, I-53100 Siena, Italy
*Correspondence author's e-mail address: ferraris@unisi.it

*(Received 2001 November 12; accepted in revised form 2002 May 29)*

**Abstract**–Sixteen texturally different (porphyritic, barred, radial, cryptocrystalline) FeO-rich chondrules from the unequilibrated ordinary chondrites Brownfield, Frontier Mountain (FRO) 90003 and FRO 90032 were characterized by optical and scanning electron microscopy and then thoroughly studied by transmission and analytical electron microscopy. Nanotextural and nanochemical data indicate similar thermal evolution for chondrules of the same textural groups; minor, yet meaningful differences occur among the different groups. Olivine is the earliest phase formed and crystallizes between 1500 and 1400 °C. Protoenstatite crystallizes at temperatures higher than 1350–1200 °C; it later inverts to clinoenstatite in the 1250–1200 °C range. Enstatite is surrounded by pigeonitic or (less frequently) augitic rims; the minimal crystallization temperature for the rims is 1000 °C; high pigeonite later inverts to low pigeonite, between 935 and 845 °C. The outer pigeonitic or augitic rims are constantly exsolved, producing sigmoidal augite or enstatite precipitates; sigmoidal precipitates record exsolution temperatures between 1000 and 640 °C. Cooling rate (determined using the speedometer based upon ortho-clinoenstatite intergrowth) was in the order of 50–3000 °C/h at the clinoenstatite–orthoenstatite transition temperature (close to 1250–1200 °C), but decreased to 5–10 °C/h or slower at the exsolution temperature (between 1000 and 650 °C), thus revealing nonlinear cooling paths. Nanoscale observations indicate that the individual chondrules formed and cooled separately from 1500 °C down to at least 650 °C. Accretion into chondritic parent body occurred at temperatures lower than 650 °C.

## INTRODUCTION

Ordinary chondrites (OC) are the most abundant meteorites. They are divided into chemical groups (H, L and LL), the H group being the most abundant and the least oxidized (*e.g.*, Van Schmus and Wood, 1967; Dodd, 1981). The major components of OCs are chondrules, matrix, metal alloys and sulfides; refractory Ca- and Al-rich inclusions (CAIs) may be present. Chondrules (0.1 to 1.0 mm in apparent diameter) consist of Mg-Fe silicates (olivine), Mg-Fe-Ca chain-silicates (pyroxenes), Si- and Al-rich glass, minor Na-K-Ca framework-silicates, Fe-Ni alloys, transition elements, sulfides, and oxides.

Because chondrules are among the most unfractioned objects in the solar system and the putative building blocks of planets, their origin is a matter of interest. It is generally accepted that chondrules formed in the solar nebula from melted droplets of still more primitive material, prior to or during accretion of planetesimals (Grossman, 1988). As chondrules show quite a range of sizes, textures, mineral abundances, mineral compositions, bulk and isotopic compositions, they potentially convey information about the chemical and physical environment of the early solar nebula, notwithstanding the difficult task of deciphering this information (Kerr, 2001).

Several experiments successfully constrained crystallization and cooling histories of chondrules (Tsuchiyama *et al.*, 1980; Hewins, 1983, 1988; Lofgren, 1983, 1989, 1996; Lofgren and Russell, 1986; Lofgren and Lanier, 1990; Connolly and Hewins, 1991; Hewins and Connolly, 1994; Kennedy *et al.*, 1993; Watanabe *et al.*, 1985; Kitamura *et al.*, 1983; Weinbruch and Müller, 1995; Jones and Layne, 1997; Weinbruch *et al.*, 2001). Owing to their rapid formation, chondrules may contain complex micro- to nanoscale textures. On the one hand, complexity makes the interpretation of bulk properties difficult. On the other hand, micro- and nanostructures may allow us to qualitatively and quantitatively derive crystallization sequences and cooling paths. These structures may be thoroughly detected and analyzed using modern transmission electron microscopy (TEM), coupled with analytical electron microscopy (AEM) techniques (*e.g.*, Ashworth, 1980, 1981; Töpel-Schadt and Müller, 1985; Brearley and Jones, 1993; Folco and Mellini, 2000).



Prelude preprint MS#4691

In this work, we report a TEM-AEM "thermospeedometric" study of primitive, unequilibrated H chondrites. In particular, these are meteorites with petrographic type ranging from 3.4 to 3.6 (Van Schmus and Wood, 1967; Sears *et al.*, 1980). To avoid later overprint, we selected meteorites as little as possible affected by post-accretional thermal metamorphism (*e.g.*, Brearley and Jones, 1993), or by collisional shock deformation (Stöffler *et al.*, 1991). Most of our attention was directed to pyroxenes, as these minerals have compositional and textural properties that are very sensitive to the time-temperature evolution. All along this paper, we generically define magnesium pyroxenes as enstatite, when the structural type (*i.e.*, orthoenstatite or clinoenstatite) is not specified

## SAMPLES AND ANALYTICAL PROCEDURES

Three different meteorites were selected amongst the most unequilibrated and unshocked specimens of the meteorite collection of the Siena Museo Nazionale dell'Antartide (Folco and Rastelli, 2000). Frontier Mountain (FRO) 90003 (FR3, henceforth) and FRO 90032 (FR32) are finds from Antarctica; Brownfield (BFR) is a find from USA. Following Sears *et al.* (1980), we classified FR32 as H3.4 and FR3 as H3.6 chondrites, while BFR had been defined H3.6 by Nehru *et al.* (1997). Following Stöffler *et al.* (1991), the shock deformation state is S1 for BFR, FR3 and FR32. The three chondrites show different weathering degrees (Wlotzka, 1993), namely W3, W2 and W1 for BFR, FR3 and FR32, respectively. Within the three meteorites, we selected several chondrules for further characterization, and finally we succeeded in analyzing 16 by TEM and AEM.

### Samples and Petrographic Analysis of the Chondrites

Three 2.7, 0.8 and 0.7 $cm^2$ wide polished thin sections, glued with thermolabile cement, were prepared from BFR, FR3 and FR32, respectively.

The three chondrites show different petrographic characteristics, particularly major components abundances. Chondrules comprise 70–75% of the BFR volume; chondrules larger than 400 $\mu$m are usually porphyritic; chondrules smaller than 150 $\mu$m are non-porphyritic (radial or barred) to cryptocrystalline. Matrix amounts to 15–20%; metal alloys and sulfides to 10–12%, respectively. Olivine grains in the matrix are normally zoned ($Fo_{96-78}$), up to 750 $\mu$m in apparent diameter. Also pyroxenes and pieces of broken chondrules occur in the matrix.

The FR3 chondrules have a mean diameter of 730 $\mu$m, amount to 80% of the volume and are mostly porphyritic. Matrix amounts to 10–15%; metal and sulfides to 5–8%, respectively. Olivines ($Fo_{82-80}$) and pyroxenes ($En_{94-83}$) occur within the matrix.

FR32 chondrules comprise 60%, are mainly porphyritic, and have mean diameter of 890 $\mu$m. Matrix comprises 20–25%, and metal and sulfides 5–10%. Normally zoned olivine grains ($Fo_{99-77}$), up to 200 $\mu$m in apparent diameter, and pyroxenes, ranging in composition from $En_{97}$ to $En_{51}Wo_1$, occur in the matrix.

Gooding and Keil (1981) texturally classified chondrules as (1) porphyritic (P), followed by letters O and/or P depending on the presence of olivine and/or pyroxene phenocrysts (PO, PP, POP), and (2) nonporphyritic, including radial and barred pyroxene (RP and BP), cryptocrystalline (C) and granular olivine-pyroxene (GOP). We focused our attention on chondrules containing at least 40–50 vol% pyroxene. Individual chondrules were selected using optical and scanning electron microscopy. In particular, we looked for porphyritic POP, and nonporphyritic RP, BP and C chondrules. We discarded BO and PO chondrules because of the expected absence of pyroxene. We also discarded GOP chondrules because of their small dimensions (<100 $\mu$m in size), as well as chondrules having more than 5–7% alloy and sulfide. Two selected chondrules with PP structure were destroyed during ion milling. A total of nine, five and two chondrules (Table 1) were selected from Brownfield (and named BFR-##), FRO 90003 (FR3-##) and FRO 90032 (FR32-##), respectively. Apparent chondrule diameters range from 140 up to 3800 $\mu$m (Fig. 1). The pictures show also the distribution of metals and sulfides particles. These appear as bright features within the chondrules; the bright contrast is due to the high average atomic number of metals and sulfides.

### Textures and Chemical Compositions of the Chondrules

All chondrules were texturally and chemically characterized using a Philips XL-30 scanning electron microscope (SEM), operating at 20 kV and equipped with an EDAX-DX4 energy dispersive spectrometer (EDS). Analyses were calibrated using silicate minerals (olivines, pyroxenes and feldspars) as reference standards. Counting rate was constantly kept close to the optimal values of 2200–2300 counts per second over the whole energy spectrum. Raw data were reduced using ZAF4 (Duncumb and Reed, 1968). The resulting values were normalized imposing 100 wt% as the sum of anhydrous oxides. Owing to the relatively simple chemical composition (only light elements with K lines), and to energy resolution of the EDS detector close to 135 eV, no major peak overlap occurred within the spectra; therefore, integrated intensities were obtained by simple best-fit deconvolution methods. Analytical precision, checked by repeated analyses of secondary standards, was better than 0.5% relative for major elements, and better than 20% relative for minor elements (*i.e.*, those with contents ranging from the minimal detectable mass of 0.3 wt% up to 3–5 wt%). Analytical accuracy has been repeatedly verified by comparison of experimentally determined and expected data for homogeneous standards; the difference is always lower than 1 wt% absolute, even for the most abundant elements (silicon) or the most difficult elements (*e.g.*, the light and mobile

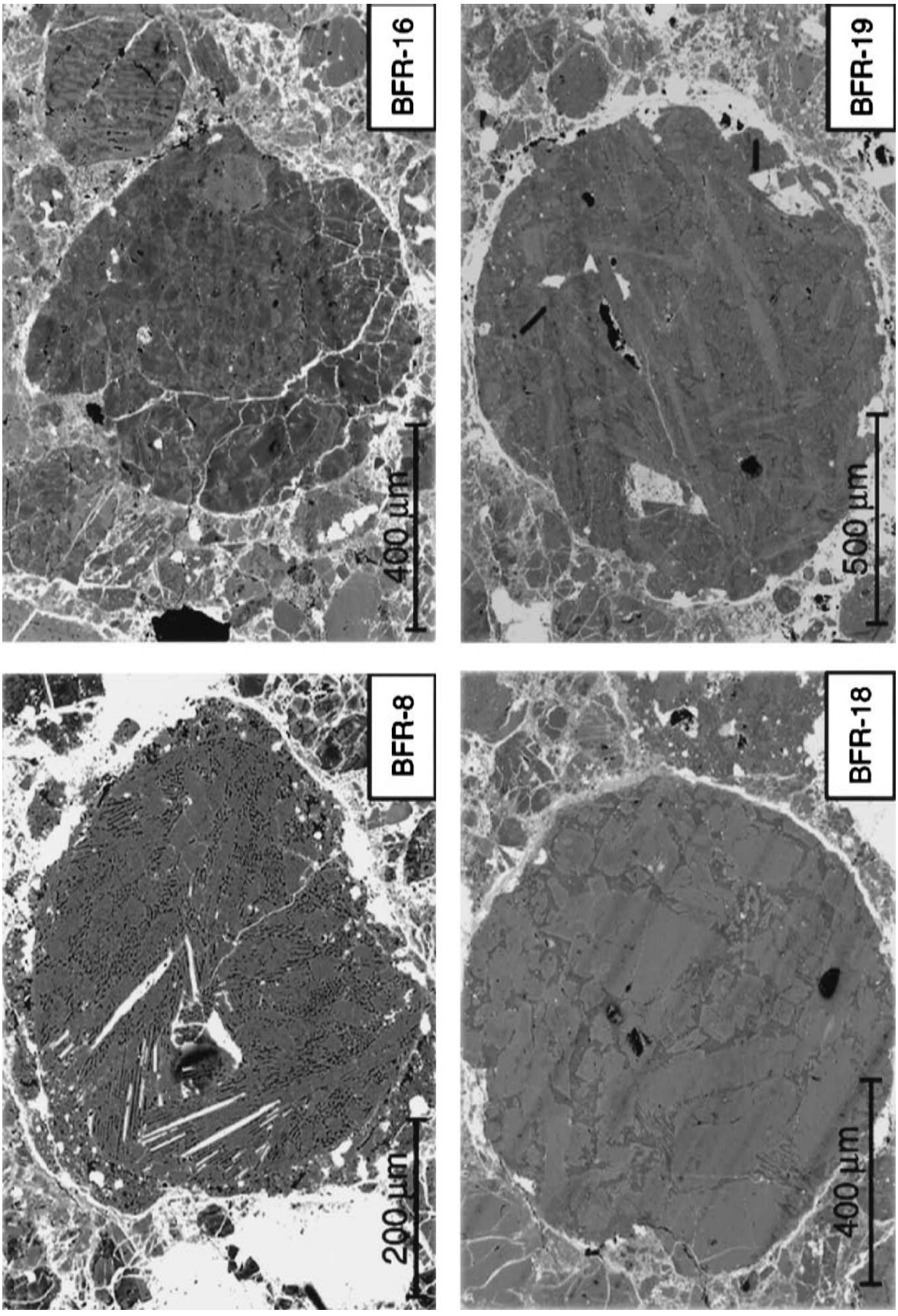


FIG. 1. SEM-BSE images of the sixteen chondrules from the Brownfield, FRO 90003 and FRO 90032 chondrites. *Figure 1 is continued on the following pages.*

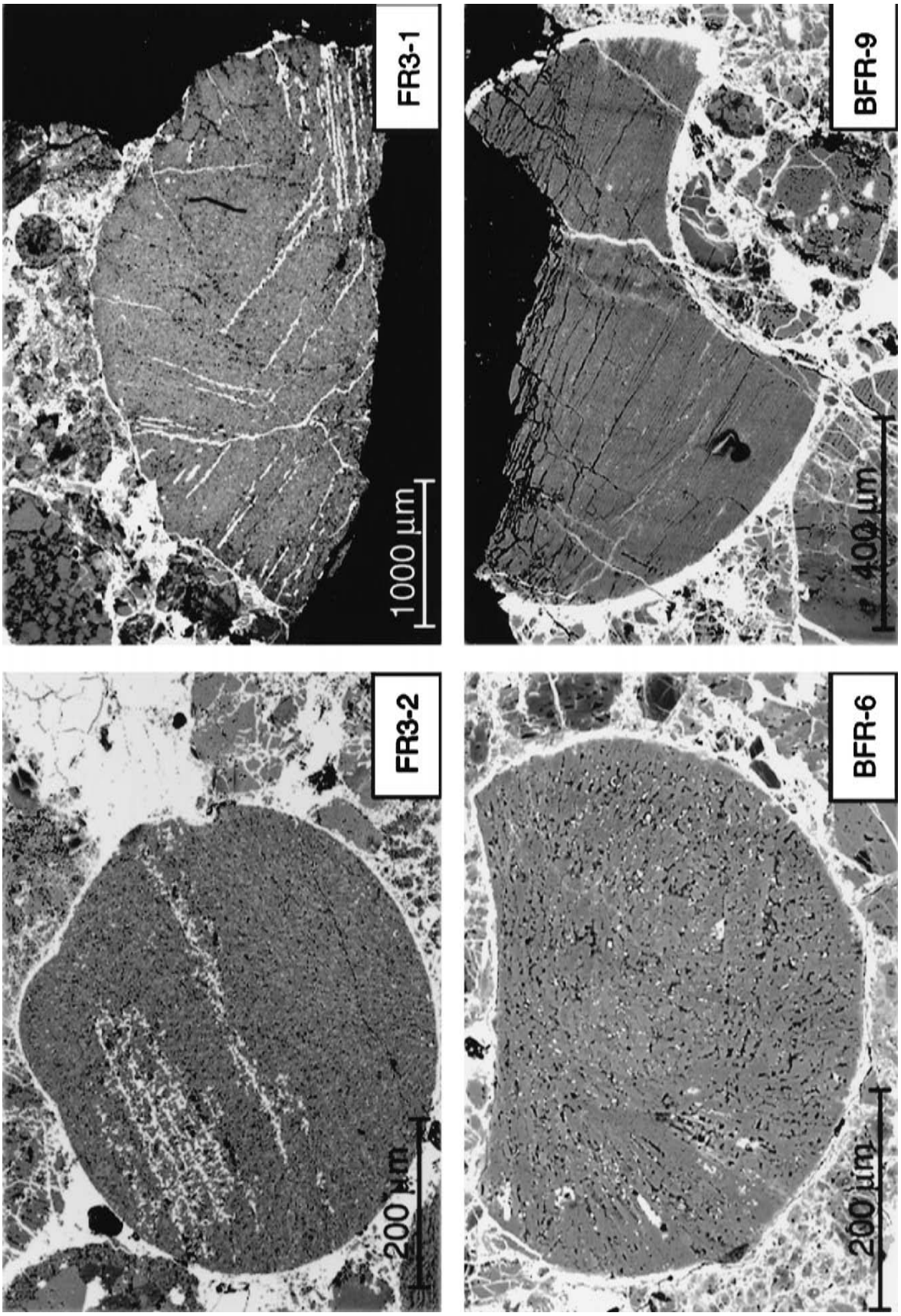


FIG. 1. *Continued.*

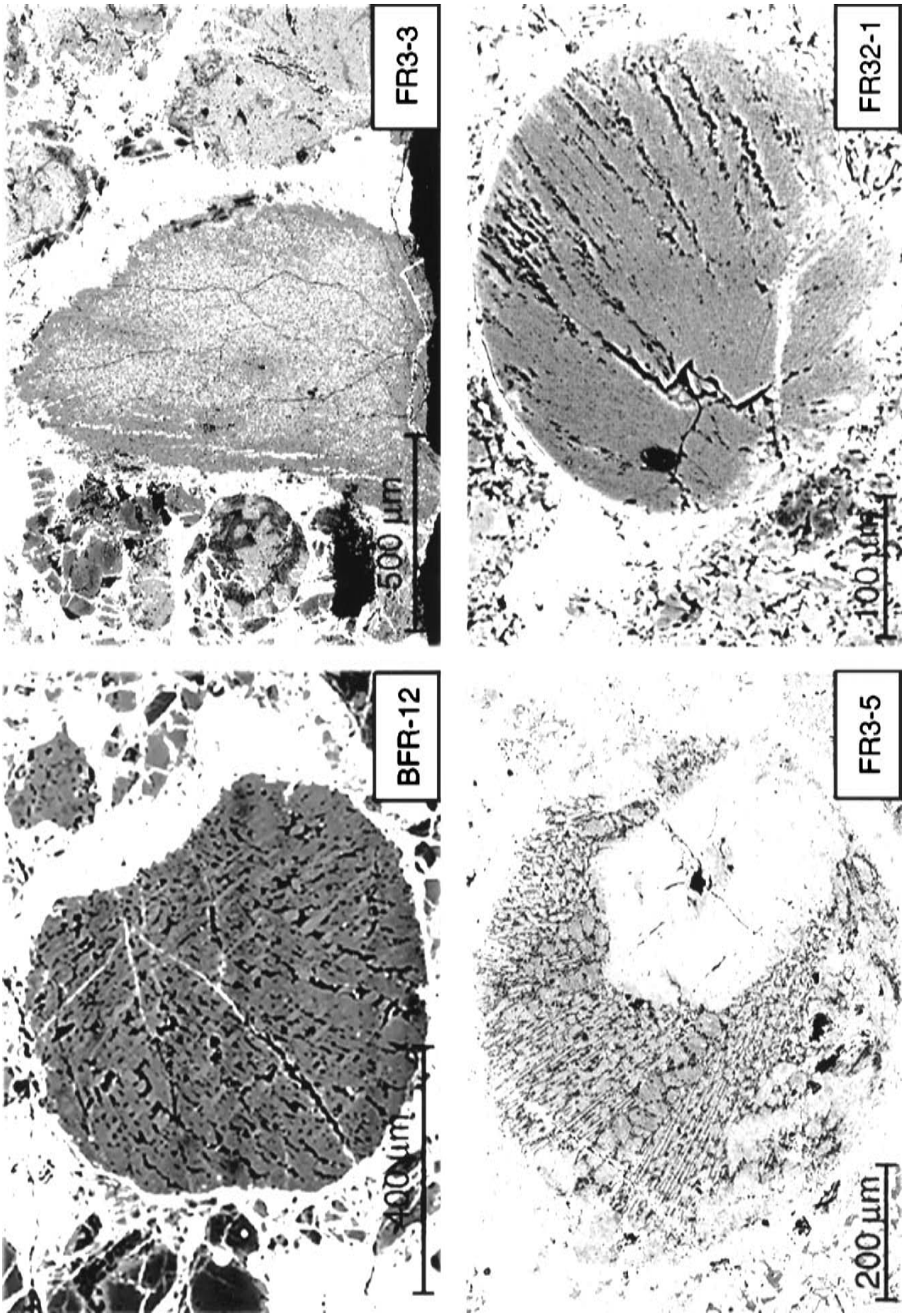


FIG. 1. *Continued.*

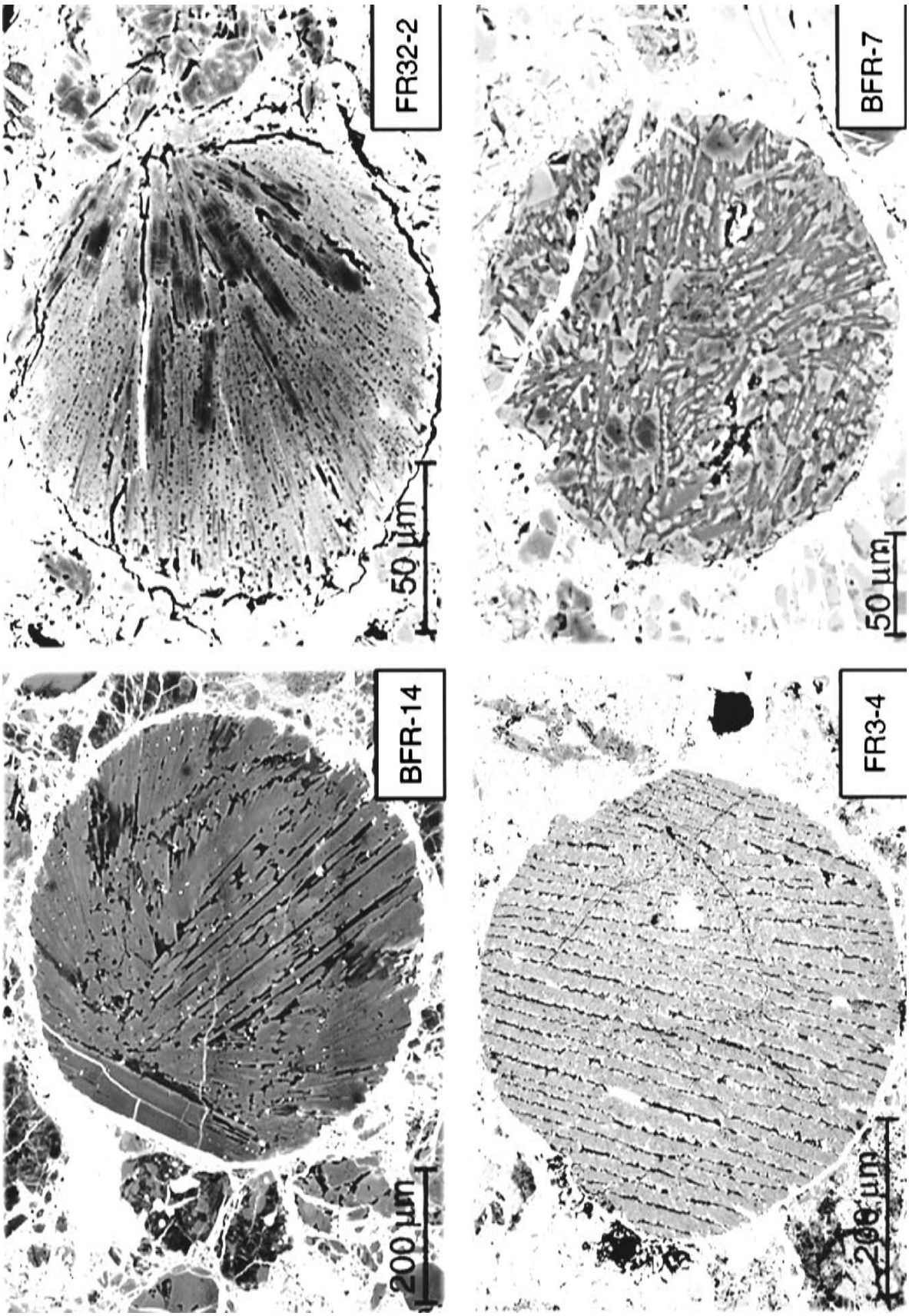


FIG. 1. *Continued.*

TABLE 1. Chemical compositions of individual chondrules, classified according to Gooding and Keil (1981) and Hewins (1997).*

| | Type IIAB | | | | | | | | Type IIB | | | | | | Ca-Al rich |
|---|---|---|---|---|---|---|---|---|---|---|---|---|---|---|---|
| | POP | | | | C | | | | C | | | RP | | BP | |
| | BFR-8 | BFR-16 | BFR-18 | BFR-19 | BFR-6 | BFR-9 | FR3-1 | FR3-2 | BFR-12 | FR3-3 | FR3-5 | FR32-1 | BFR-14 | FR32-2 | FR3-4 | BFR-7 |
| $SiO_2$ | 46.1 | 53.9 | 50.2 | 53.8 | 51.2 | 50.8 | 52.9 | 50.6 | 54.7 | 58.2 | 57.3 | 55.8 | 57.8 | 57.6 | 56.8 | 55.2 |
| $Al_2O_3$ | 3.2 | 4.4 | 4.1 | 4.0 | 3.2 | 2.9 | 3.3 | 3.0 | 3.9 | 2.6 | 4.3 | 3.5 | 2.9 | 2.7 | 3.6 | 15.6 |
| $Cr_2O_3$ | 0.2 | 0.3 | 0.3 | 0.3 | 0.2 | 0.5 | 0.1 | 0.2 | 0.3 | 0.1 | 0.2 | 0.1 | 0.2 | 0.2 | 0.3 | 0.0 |
| $TiO_2$ | 0.3 | 0.1 | 0.2 | 0.2 | 0.1 | 0.1 | 0.1 | 0.2 | 0.1 | 0.1 | 0.1 | 0.1 | 0.1 | 0.1 | 0.1 | 0.2 |
| MgO | 28.6 | 26.7 | 27.0 | 25.7 | 25.2 | 24.4 | 23.1 | 26.2 | 24.2 | 21.5 | 24.8 | 26.9 | 23.2 | 29.6 | 25.1 | 11.5 |
| FeO | 17.3 | 11.3 | 13.4 | 12.4 | 16.3 | 16.8 | 17.2 | 16.4 | 13.3 | 13.4 | 9.7 | 10.6 | 12.7 | 7.7 | 10.8 | 5.3 |
| MnO | 0.3 | 0.2 | 0.3 | 0.2 | 0.2 | 0.4 | 0.2 | 0.2 | 0.3 | 0.3 | 0.2 | 0.2 | 0.2 | 0.1 | 0.2 | 0.0 |
| NiO | 0.2 | 0.3 | 0.2 | 0.2 | 0.1 | 0.1 | 0.1 | 0.2 | 0.0 | 0.0 | 0.1 | 0.1 | 0.1 | 0.0 | 0.0 | 0.1 |
| CaO | 2.5 | 2.1 | 2.6 | 2.0 | 2.1 | 2.3 | 2.1 | 2.3 | 1.9 | 2.9 | 1.8 | 1.8 | 1.8 | 1.6 | 1.6 | 10.9 |
| $Na_2O$ | 1.2 | 0.7 | 1.3 | 1.2 | 1.2 | 1.5 | 0.9 | 0.7 | 1.2 | 0.9 | 1.4 | 0.9 | 0.8 | 0.4 | 1.1 | 1.2 |
| $K_2O$ | 0.1 | 0.0 | 0.4 | 0.0 | 0.2 | 0.2 | 0.0 | 0.0 | 0.0 | 0.0 | 0.1 | 0.0 | 0.2 | 0.0 | 0.0 | 0.0 |
| FeO/MgO | 0.6 | 0.4 | 0.5 | 0.5 | 0.6 | 0.7 | 0.7 | 0.6 | 0.5 | 0.6 | 0.4 | 0.4 | 0.5 | 0.3 | 0.4 | 0.5 |
| Maximal size ($\mu$m) | 540 | 550 | 870 | 1240 | 530 | 1070 | 3800 | 1080 | 370 | 1960 | 790 | 320 | 430 | 140 | 970 | 230 |

*BFR chondrules are from Brownfield; FR3 from FRO 90003; FR32 from FRO 90032. Compositions are given as wt% and normalized to a total of 100 wt%.

sodium); otherwise, the observed expected difference is definitely lower than 1 wt%.

Mean chondrule compositions (Tables 1 and 2) were obtained by raster analyses of areas extending from 0.01 to 0.25 $mm^2$. Eleven different chemical components were determined ($SiO_2$, $Al_2O_3$, $Cr_2O_3$, $TiO_2$, MgO, FeO, MnO, NiO, CaO, $Na_2O$, $K_2O$) and the chemical analyses were normalized to 100 wt%. Repeated analyses from the same regions led to homogeneous values, reproducible within the previously discussed analytical precision. Following the chemical classification of chondrules proposed by McSween (1977) and modified by Scott and Taylor (1983), Jones (1994), Hewins (1997), 15 of our samples belong to the most abundant chondrule type in OC (type II, FeO-rich chondrules; Grossman *et al.*, 1988; Brearley and Jones, 1998) and may be defined by letters A and/or B in the presence of olivine and/or pyroxene, respectively (Table 1). Only one of the 16 chondrules (BFR-7) differs from the type II population, being a Ca-Al-rich chondrule, a rare constituent of OC (Grossman *et al.*, 1988; Brearley and Jones, 1993).

Imaging was mostly done using composition-dependent, backscattered electrons (BSE). The overall SEM-EDS-BSE investigation was focused to define both mean chemical compositions of chondrules, and textures and compositions of minerals and glass within each chondrule.

## High-Resolution Transmission Electron Microscopic Imaging and Analytical Electron Microscopic Nanoprobe

After SEM-EDS-BSE analyses, TEM specimens were prepared gluing appropriate single hole copper grids on each chondrule. After mechanical polishing, specimens were ion-thinned by argon milling (progressively decreasing from 5 to 1.5 kV acceleration voltage) and coated with a 5 nm carbon film.

HRTEM and AEM investigations were performed at 200 kV on a JEOL JEM 2010 electron microscope equipped with double-tilt holder, $LaB_6$ cathode, LH72 WA-TEM TV-rate camera, and LINK ISIS EDS x-ray microanalysis. Field limiting apertures used for selected area electron diffraction (SAED) were 5, 20, and 60 $\mu$m in diameter. High-resolution images were collected using a high contrast objective aperture of 20 $\mu$m, corresponding to a nominal point-to-point resolution of 0.19 nm.

AEM investigations were performed in TEM-EDS mode, with live counting time of 30 s; the very fine beam diameter (1 to 10 nm) was defocused for glasses and feldspars to more than 25 nm in order to reduce alkalies loss. Recalculation and normalization of the AEM analyses were performed assuming thin-film approximation, using experimental calibrations from silicate standards. AEM compositions were expressed based upon 4, 6 and 8 oxygen atoms per formula unit (a.p.f.u.) for olivine, pyroxene and feldspar, respectively, and assuming ferrous iron. Glass AEM compositions were recalculated on the basis of cation ratios, fixing the sum of (Ca + Al + Na + K)

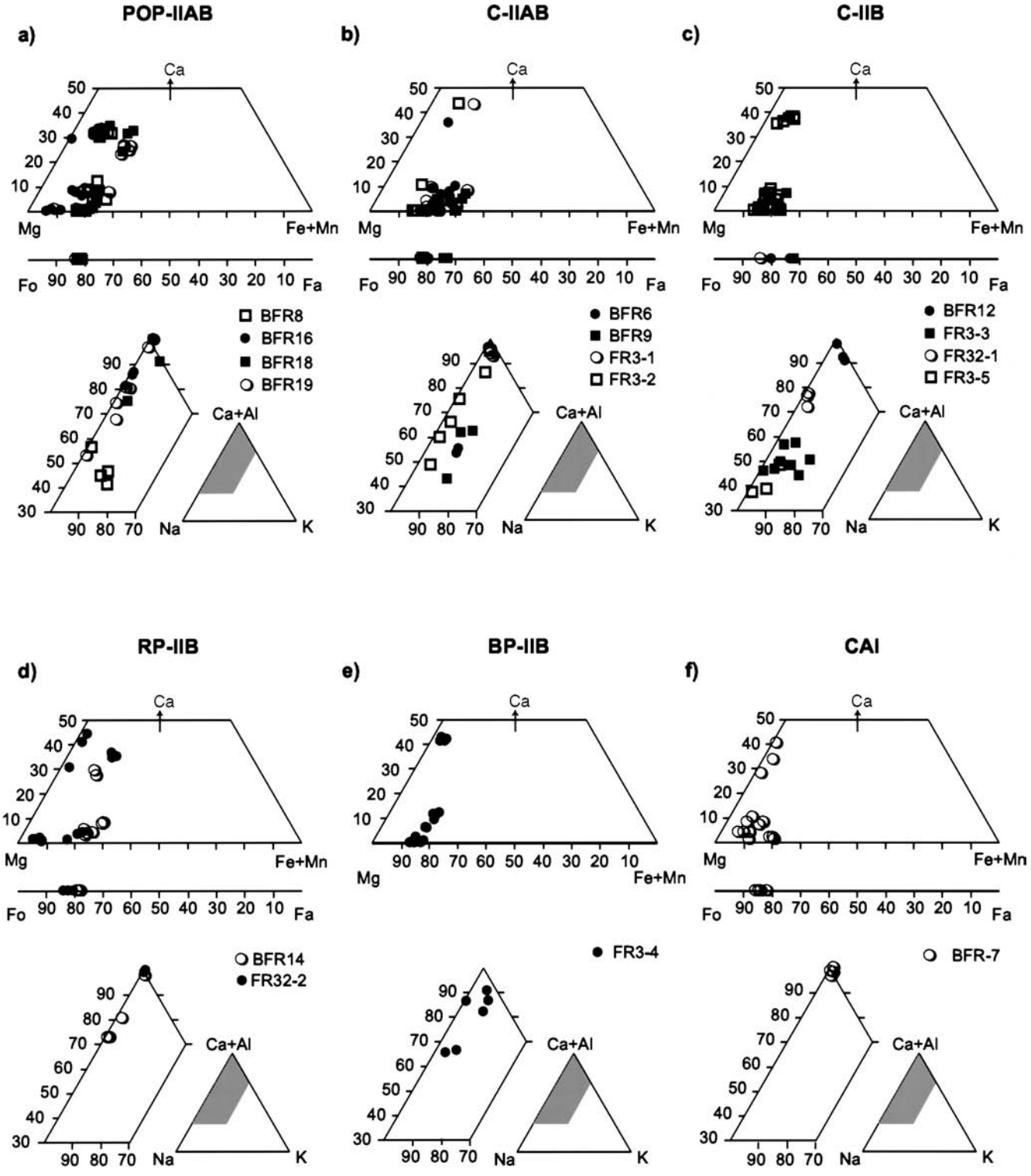


FIG. 2. Mineral chemistry (AEM data) for chondrule pyroxenes (upper quadrilateral), olivines (central line) and glass (lower quadrilateral): (a) POP; (b) C-IIAB; (c) C-IIB; (d) RP-IIB; (e) BP-IIB; (f) CAI.

TABLE 2. Average chemical compositions of chondrules belonging to different textural groups*.

| | POP-IIAB | | C (IIAB) | | C (IIB) | | RP (IIB) | | BP (IIB) |
|---|---|---|---|---|---|---|---|---|---|
| $SiO_2$ | 51.0 | (3.8) | 51.4 | (1.0) | 56.5 | (1.6) | 57.7 | (0.2) | 56.8 |
| $Al_2O_3$ | 3.9 | (0.5) | 3.2 | (0.2) | 3.6 | (0.7) | 2.8 | (0.1) | 3.7 |
| $Cr_2O_3$ | 0.3 | (0.1) | 0.2 | (0.1) | 0.2 | (0.1) | 0.2 | (0.1) | 0.3 |
| $TiO_2$ | 0.2 | (0.1) | 0.2 | (0.1) | 0.1 | (0.1) | 0.1 | (0.1) | 0.1 |
| MgO | 27.0 | (1.2) | 24.8 | (1.3) | 24.4 | (2.3) | 26.4 | (4.5) | 25.1 |
| FeO | 13.9 | (3.1) | 16.6 | (0.4) | 11.8 | (1.9) | 10.2 | (3.5) | 10.8 |
| MnO | 0.2 | (0.1) | 0.2 | (0.1) | 0.1 | (0.1) | 0.1 | (0.1) | 0.2 |
| NiO | 0.2 | (0.0) | 0.1 | (0.1) | 0.1 | (0.1) | 0.1 | (0.1) | 0.1 |
| CaO | 2.1 | (0.4) | 2.2 | (0.1) | 2.0 | (0.4) | 1.7 | (0.1) | 1.7 |
| $Na_2O$ | 1.1 | (0.2) | 1.0 | (0.3) | 1.1 | (0.2) | 0.6 | (0.3) | 1.1 |
| $K_2O$ | 0.1 | (0.2) | 0.1 | (0.1) | 0.1 | (0.1) | 0.1 | (0.1) | 0.1 |
| FeO/MgO | 0.5 | | 0.7 | | 0.5 | | 0.4 | | 0.4 |

*Compositions are given as wt% and normalized to a total of 100 wt%. Mean squared deviations in parentheses.
Abbreviations: POP = porphyritic–olivine pyroxene; C = cryptocrystalline; RP = radial pyroxene; BP = barred pyroxene.

to 100. In particular, compositional profiles were obtained for zoned enstatites by line scan through the whole crystals; usually, the zoning pattern had minimal Wo content in the core.

AEM allowed us to discriminate pigeonite from clinoenstatite. Although the two phases have common $P2_1/c$ space group, they may be distinguished based upon the different calcium contents, with pigeonite having more than 0.10 calcium atoms per formula unit.

## RESULTS

### Chemical Compositions of Chondrules

Chondrule compositions are reported in Tables 1 and 2. Fifteen of the 16 chondrules share a common compositional range, typical of type II chondrules; only BFR-7 has much higher Ca and Al contents and will be described as Ca-Al-rich chondrule.

Type II chondrules show a negative correlation of $SiO_2$ *vs.* (MgO + FeO) and CaO contents, with BFR-8 and FR3-3 as extremes. These chemical patterns are closely related to the chondrule classification. In particular, the lowest the $SiO_2$ content the lowest the pyroxene content. With respect to type II chondrules, the Ca-Al rich BFR-7 chondrule has a 4–5× higher CaO and $Al_2O_3$ content (10.9 *vs.* 2.1 wt% for CaO, and 15.6 *vs.* 3.4 wt% for $Al_2O_3$) and lower $Cr_2O_3$, FeO and MgO contents (0.0 *vs.* 0.2 wt% for $Cr_2O_3$, 5.3 *vs.* 13.3 wt% for FeO and 11.5 *vs.* 25.5 wt% for MgO). No manganese or potassium was detected; Ti and Na contents do not differ from type II chondrules.

### Mineral Chemistry and Nano- to Microstructures in Type II and Calcium-Aluminum-Rich Chondrules

All chondrules contain abundant enstatite (mostly clinoenstatite faulted by orthoenstatite lamellae) mantled by discontinuous pigeonitic or augitic rims, a few micrometers in thickness. These rims show exsolved textures in ~50% of the studied chondrules. Euhedral augite is rare. In POP chondrules, minor augite and pigeonite also occur as quench crystallites within the glassy mesostasis.

Tables 3 and 4 report representative AEM compositions of the minerals observed in FeO-rich and the Ca-Al-rich chondrules, respectively.

**Porphyritic–Olivine Pyroxene IIAB**–These chondrules show different textural features (Fig. 1). Coarse-grained crystals occur in BFR-16, BFR-18 and BFR-19. Euhedral olivine and enstatite crystals range from 150 to 400 $\mu$m and from 50 to 200 $\mu$m in size. Euhedral olivines may include kamacite blebs. Olivine grains in BFR-16 show resorption textures. BFR-8 contains coarse-grained enstatites ~150 $\mu$m in size, while the abundant olivine is skeletal and smaller than 10 $\mu$m.

Olivine has homogeneous compositions in the $Fo_{81-83}$ range (Fig. 2a); limited normal zoning occurs only in BFR-8 and BFR-18 olivines, with $Fo_{85}$ cores and $Fo_{81-82}$ rims. The MnO content may be as high as 0.2 wt% in BFR-18 and BFR-19.

The enstatite AEM composition ranges from $En_{92}Wo_1$ in BFR-16 to $En_{79}Wo_3$ in BFR-8 (Fig. 2a). Discontinuous pigeonitic rims, a few micrometers thick, typically mantle enstatite. Pigeonites range from $En_{74}Wo_{10}$ in BFR-19 to $En_{76}Wo_5$ in BFR-18. TEM indicates that enstatite consists of finely intergrown orthoenstatite and clinoenstatite polymorphs. As described by Iijima and Buseck (1975), intergrown clinoenstatite and orthoenstatite are distinguished in TEM [010] lattice images because of the different $a$ periodicities (9 and 18 Å, respectively). An example of zoned structural disorder is shown in Fig. 3; proceeding towards the pigeonitic rim, the orthoenstatite content increases from 5 to 15 vol%; the highest the orthoenstatite content, the highest the apparent disorder. In the electron diffraction pattern, this feature appears as faint streaking along $a^*$ in

TABLE 3. AEM chemical compositions of chondrule minerals and crystallization temperatures.

| | Olivine* | En-core* | Pigeonite rim* | Exsolved rim (pre-exsolution) | Exsolved structure* | High-Ca pyroxene* | Feldspars and plagioclases† | Accessory phases |
|---|---|---|---|---|---|---|---|---|
| **Porphyritic–Olivine Pyroxene IIAB** | | | | | | | | |
| BFR-8 | 1506–1494 | 1219 | 1041 | 1031 | 758 ± 65 | – | 750 | – |
| | ($Fo_{85-81}$) | ($En_{79.2}Wo_{3.3}$) | ($En_{75.1}Wo_{8.8}$) | ($En_{74}Wo_{12}$) | ($En_{80-59.8}Wo_{2-28.4}$) | | ($Ab_{75}An_6Or_{19}$) | |
| BFR-16 | 1423 | 1216 | 1061 | – | – | 1000 | 1280 | – |
| | ($Fo_{83}$) | ($En_{92.5}Wo_{0.8}$) | ($En_{78.1}Wo_{8.1}$) | | | ($En_{70.2}Wo_{29.8}$) | ($Ab_{50}An_{50}$) | |
| BFR-18 | 1474–1460 | 1295 | 1239 | 1017 | 640 ± 91 | 1066 | – | – |
| | ($Fo_{85-82}$) | ($En_{80.5}Wo_{1.5}$) | ($En_{76.2}Wo_5$) | ($En_{72}Wo_{10}$) | ($En_{77.1-54.8}Wo_{1.1-34.5}$) | ($En_{40.5}Wo_{33}$) | | |
| BFR-19 | 1433 | 1271 | 1023 | – | – | – | 750 | |
| | ($Fo_{83}$) | ($En_{83.6}Wo_{0.7}$) | ($En_{73.7}Wo_{10.3}$) | | | | ($Ab_{76}An_{16}Or_8$) | Pentlandite troilite |
| **Cryptocrystalline IIAB** | | | | | | | | |
| BFR-6 | 1474–1465 | 1297 | 1041 | 1021 | 856 ± 99 | – | – | – |
| | ($Fo_{83-81}$) | ($En_{81}Wo_{0.7}$) | ($En_{76}Wo_9$) | ($En_{72}Wo_{12}$) | ($En_{79.3-52.3}Wo_{2.2-37.4}$) | | | |
| BFR-9 | 1470–1454 | 1319 | 1037 | – | – | – | – | Kamacite (2% Ni) |
| | ($Fo_{83-80}$) | ($En_{78.1}Wo_{2.3}$) | ($En_{70}Wo_{8.5}$) | | | | | |
| FR3-1 | 1445 | 1258 | 967 | 983 | 881 ± 156 | – | 750–800 | Kamacite (5% Ni) |
| | ($Fo_{74}$) | ($En_{69.9}Wo_{1.2}$) | ($En_{62.8}Wo_{11.2}$) | ($En_{63}Wo_{13}$) | ($En_{70-41}Wo_{3-44}$) | | ($Ab_{73}An_8Or_{19}$) | Troilite |
| FR3-2 | 1473 | 1260 | 1050 | 1025 | 914 ± 88 | – | 600–650 | – |
| | ($Fo_{82}$) | ($En_{84.3}Wo_{1.1}$) | ($En_{74.3}Wo_{8.3}$) | ($En_{76.5}Wo_{14.6}$) | ($En_{74.3-44.6}Wo_{4-44.9}$) | | ($Ab_{90}An_8Or_2$) | |
| **Cryptocrystalline IIB** | | | | | | | | |
| BFR-12 | 1442–1440 | 1344 | 1179 | – | – | – | – | Cr-rich spinel |
| | ($Fo_{81-74}$) | ($En_{77.5}Wo_{1.4}$) | ($En_{76.3}Wo_{5.6}$) | | | | | |
| FR3-3 | – | 1266 | 1029 | – | – | 1072 | – | – |
| | | ($En_{83.3}Wo_{1.3}$) | ($En_{74.8}Wo_{10}$) | | | ($En_{52}Wo_{39.2}$) | | |
| FR3-5 | 1470 | 1242 | 1084 | – | – | 1187 | 650 | – |
| | ($Fo_{83}$) | ($En_{86.3}Wo_{1.2}$) | ($En_{79.9}Wo_{7.2}$) | | | ($En_{57.8}Wo_{36.8}$) | ($Ab_{72}Or_{28}$) | |
| FR32-1 | 1459 | 1257 | 1109 | – | – | – | – | – |
| | ($Fo_{84}$) | ($En_{84.4}Wo_{1.2}$) | ($En_{77.3}Wo_{6.6}$) | | | | | |
| **Radial Pyroxene IIB** | | | | | | | | |
| BFR-14 | 1414–1412 | 1366 | 1009 | 1074 | 1018 ± 81 | – | – | Kamacite (3% Ni) |
| | ($Fo_{84-80}$) | ($En_{76}Wo_{2.5}$) | ($En_{70.4}Wo_{10.1}$) | ($En_{67}Wo_{17}$) | ($En_{52.6-72.7}Wo_{30.6-4.8}$) | | | |
| FR32-2 | 1404–1400 | 1202 | 1133 | 1191 | 970 ± 32 | 1006 | – | – |
| | ($Fo_{85-81}$) | ($En_{94.1}Wo_{1.3}$) | ($En_{78.4}Wo_6$) | ($En_{63}Wo_{32}$) | ($En_{53-93}Wo_{43.8}$) | ($En_{41}Wo_{37.5}$) | | |
| **Barred Pyroxene IIB** | | | | | | | | |
| FR3-4 | – | 1262 | 1050 | 1069 | 890 ± 127 | 957 | 650 | Kamacite (4%Ni) |
| | | ($En_{84.5}Wo_{0.5}$) | ($En_{76.5}Wo_{8.5}$) | ($En_{66}Wo_{17}$) | ($En_{72.5-52.2}Wo_{11-43.6}$) | ($En_{52.1}Wo_{43.6}$) | ($Ab_{88}An_6Or_6$) | Troilite |

*Minimal crystallization temperatures (°C).

†Minimal and maximal crystallization temperatures (°C) for feldspars and plagioclases, respectively.

TABLE 4. AEM chemical compositions of Ca-Al rich chondrule minerals and crystallization temperatures.

| | Olivine* | Relic enstatite core* | Relic pigeonite rim* | Relic exsolved rim (pre-exsolution) | Relic exsolved texture* | Enstatite core* | Pigeonite rim* | Exsolved rim* (pre-exsolution) | Exsolved structure* | Plagioclases† |
|---|---|---|---|---|---|---|---|---|---|---|
| BFR-7 | 1400 ($Fo_{87-83}$) | 1182 ($En_{89.5}Wo_{3.3}$) | 1091 ($En_{85.9}Wo_8$) | 1192 ($En_{56.8}Wo_{35.6}$) | 964 ± 64 ($En_{57.5-86.8}Wo_{41.7-4.5}$) | 1295 ($En_{80.1}Wo_{1.8}$) | 1066 ($En_{81.8}Wo_{8.4}$) | 1268 ($En_{68.7}Wo_{27.8}$) | 1067 ± 65 ($En_{60.6-84.3}Wo_{39.4-5.2}$) | 1400–1280 ($Ab_{70-54}$) 1550 ($An_{100}$) |

*Minimal crystallization temperatures (°C).
†Minimal and maximal crystallization temperatures (°C) for feldspars and plagioclases, respectively.

the cores and by additional orthoenstatite spots in the rims (insets of Fig. 3a,b).

In two of the four POP chondrules (BFR-8 and BFR-18), the outermost part of the pigeonitic rim is exsolved. The exsolution texture, rather than lamellar association or spinodal decomposition, consists of augitic sigmoidal precipitates exsolved within a clinoenstatite matrix (Fig. 4). In particular, the exsolved rim shows (1) straight, parallel (100) orthoenstatite lamellae cutting through the host clinoenstatite structure; (2) iso-aligned augite sigmoids, lying roughly at 45° from the 18 Å lamellae. Average AEM analyses from wide areas, gathered using defocused beams, indicate pre-exsolution compositions of $En_{74}Wo_{12}$ and $En_{72}Wo_{10}$, for BFR-8 and BFR-18, respectively. Focused nanobeams identify the sigmoids as $En_{60}Wo_{28}$ and $En_{55}Wo_{35}$ augites within $En_{80}Wo_2$ and $En_{77}Wo_1$ (BFR-8 and BFR-18, respectively) clinoenstatite hosts. The average, pseudoperiodic spacing of the exsolution texture ($\lambda$) (*e.g.*, Brizi and Mellini, 1992) is 36–37 nm, measured as the average distance along [001] between adjacent augite sigmoids. The mean width of sigmoids ($\sigma$) measured along the same direction is ~13 nm.

The chondrules BFR-16 and BFR-18 also contain 100 $\mu$m large, porphyritic pyroxenes with augitic compositions $En_{70}Wo_{30}$ and $En_{41}Wo_{33}$, respectively.

POP chondrules also contain 1 to 5 $\mu$m acicular and/or skeletal crystals, occurring within the glass (Fig. 5). Most of these pyroxenes are augites ($En_{53}Wo_{27}$); for chondrule BFR-8, we observed $En_{71}Wo_6$ pigeonite needles.

Glass is chemically heterogeneous, either from chondrule to chondrule or within the same chondrule, with silicon between 63 and 88 of the total cations, and aluminum between 26 and 4%. The BFR-8 chondrules (Fig. 2a) have the highest alkalies content; conversely, BFR-16 and BFR-18 chondrules are alkalies-depleted. The BFR-19 glass shows wide compositional variations, depending on textural setting; namely, the glass is Na-depleted when located between Ca-rich pyroxenes, and Na- and K-enriched when located between low-Ca pyroxenes and/or olivines. The BFR-19 glass also contains Cr-rich spinel, troilite, pentlandite and feldspar; feldspar and/or plagioclase are also common within the BFR-8 and BFR-16 glasses.

**Cryptocrystalline IIAB**–The C IIAB chondrules are richest in FeO (Table 2). They also are the largest, with an average apparent diameter of ~1600 $\mu$m (Fig. 1).

The chondrules FR3-1, FR3-2 and BFR-6 have different textures. Both FR3 chondrules show anhedral olivines and enstatite, 5 to 20 $\mu$m in size; BFR-6 has euhedral olivine grains, 10 $\mu$m in size. BFR-9 is coarse-grained with acicular olivine crystals, 1–5 $\mu$m in width and 20–100 $\mu$m in length; the enstatite, 1 to 10 $\mu$m in size, grows around olivine crystals and shows mottled contrast in bright field images (Fig. 6), similar to the contrast shown by antiphase domains (Morimoto and Tokonami, 1969; Heuer and Nord, 1976; Carpenter, 1979).

The BFR-6 and BFR-9 olivines are slightly zoned, with $Fo_{83}$ cores and $Fo_{81-80}$ rims (Fig. 2b); FR3-1 and FR3-2 olivines

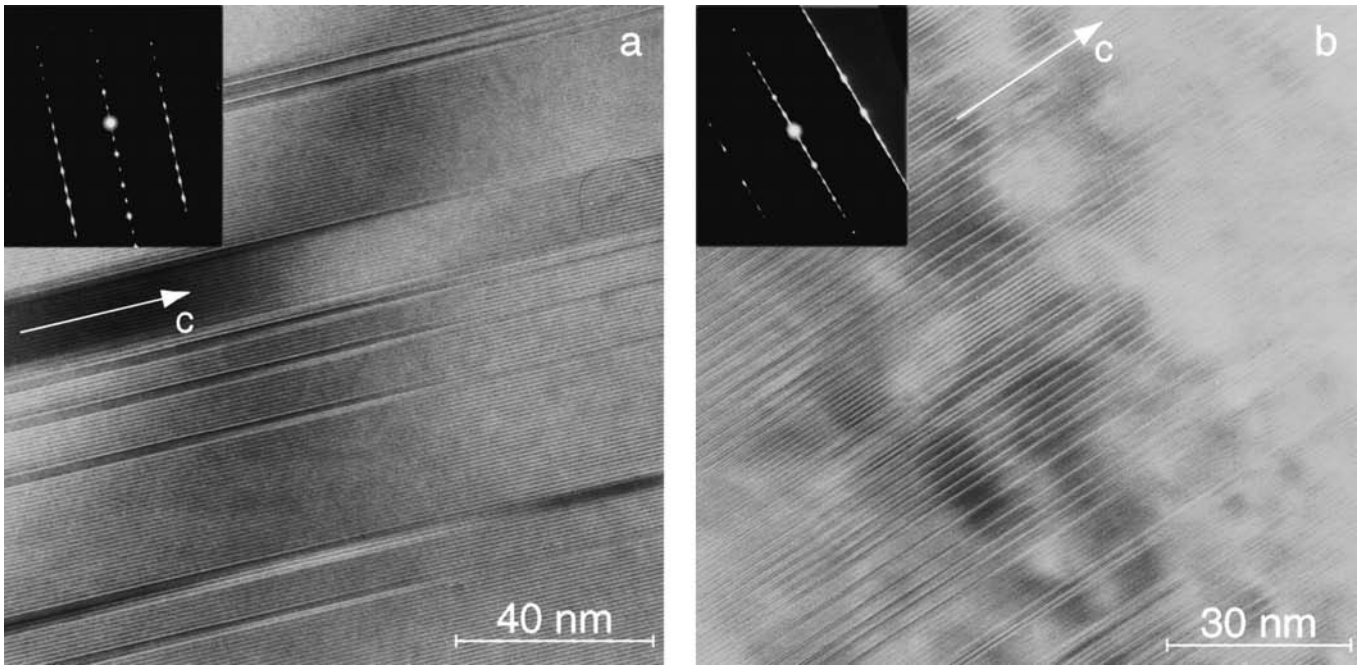


FIG. 3. Orthoenstatite–clinoenstatite association in enstatite from POP chondrules: (a) (100) orthoenstatite–clinoenstatite lamellar association present at the core; (b), (100) orthoenstatite–clinoenstatite lamellar association at the periphery. [100] stacking disorder increases toward the outer part of the crystal as also shown in the electron diffraction pattern.

are homogeneous, with $Fo_{74}$ and $Fo_{82}$ compositions, respectively. The MnO content of olivine (mean value of 0.1 wt%) is lower than in the previous POP IIAB group; only olivines in the FR3-1 chondrule reach 0.2 wt% MnO. No mineral inclusions occur within the olivine grains.

Pyroxene chemistry is simpler than for the POP IIAB group (Fig. 2b). Pyroxene crystals consist of zoned enstatites $En_{84}Wo_1$ to $En_{70}Wo_1$, mantled by pigeonitic rims up to $En_{63}Wo_{11}$ in FR3-1. Orthoenstatite/clinoenstatite disorder is qualitatively similar to POP IIAB group; however, the orthoenstatite content increases from 14 to 21% towards the crystal rim.

Apart from BFR-9, all the C IIAB chondrules have exsolved pigeonitic external rims. Also in this case the exsolution texture consists of augite sigmoids exsolved from pigeonite. Average pre-exsolution AEM compositions of the rim (Fig. 2b) indicate similar pigeonitic compositions in FR3-1 and FR3-2 ($En_{63}Wo_{13}$ and $En_{67}Wo_{15}$), whereas BFR-6 is richer in Mg ($En_{72}Wo_{12}$). The sigmoids have similar compositions in FR3-1 and FR3-2, $En_{41}Wo_{44}$ and $En_{45}Wo_{45}$, respectively, but become richer in Mg and poorer in Ca in BFR-6 ($En_{52}Wo_{37}$). The sigmoids lay at 45° from the orthoenstatite lamellae that cut the clinoenstatite matrix. The $\sigma$ value is 7.5 nm and $\lambda$ is 18 nm. More complex pattern characterizes BFR-6. BFR-6 shows well-evident [100] twinned structure (vertical bands in Fig. 7). Augite sigmoids alternate each to the other in twin-related orientation. As a consequence, textures indicate that the exsolved sigmoids are subsequent to the [100] twinned structure, originated during the high-pigeonite to low-pigeonite transition (expected to occur between 935 and 845 °C; Schröpfer, 1985).

The C IIAB glasses recall the POP IIAB group (Fig. 2b). Compositions are heterogeneous (both from chondrule to chondrule in the same chondrite and within the given chondrule); two groups may be discriminated by the different K contents. The first group (BFR-6 and BFR-9) is K-enriched; FR3-2 has low K content and FR3-1 no alkalies. The two groups display variable Ca + Al contents. The chemical differences vary according to textural setting. Na-depletion occurs within micrometric glass pockets located between olivine and low-Ca pyroxene grains; in these sites, we also found bytownitic-andesitic plagioclase ($Ab_{30}$), which explains the local Ca- and Al-enrichments, together with chromite, troilite and kamacite. Otherwise, Na-enrichment occurs for glass present as submicrometric thin films located between olivine and pyroxene grains.

Kamacite occurs within the BFR-9 and FR3-1 glasses, with 2 and 5% of Ni, respectively.

**Cryptocrystalline IIB**–C IIB chondrules are $SiO_2$-richer (56.5 wt% for C IIB, 56.9 wt% for BP IIB and 57.7 wt% for RP IIB), and FeO-, NiO-, $TiO_2$- and $K_2O$-depleted with respect to C IIAB chondrules (Table 2).

C IIB chondrules may be texturally heterogeneous (Fig. 1). FR3-3 and FR32-1 are fine-grained with anhedral enstatite grains (again clinoenstatite + orthoenstatite), 5 to 20 $\mu$m in size and (FR32-1 only) submicrometer skeletal olivine crystals with

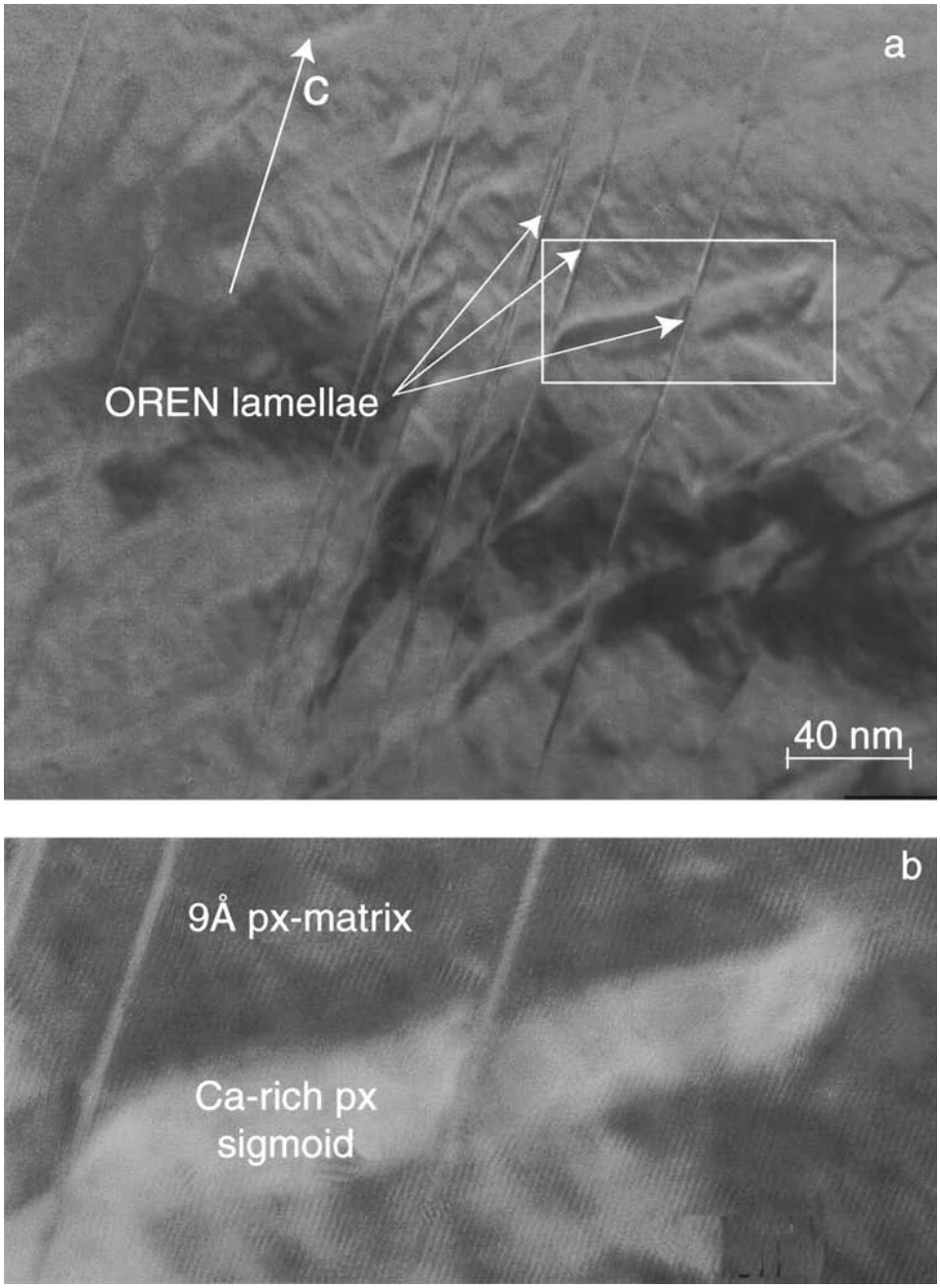


FIG. 4. TEM images of exsolution textures in pigeonitic rims in POP chondrules: (a) a few straight and sharp 18 Å lamellae cut across the 9 Å matrix, at high angles from iso-aligned augite sigmoids; (b) enlarged view of orthoenstatite–clinoenstatite–augite sigmoids relationships, same area as the box drawn in (a).

$Fo_{84}$ homogeneous composition. FR3-5 has a coarse-grained texture, characterized by aggregates of enstatite crystals 20 to 30 $\mu$m in size and by both acicular and euhedral olivine crystals 100 and 300 $\mu$m in length and in mean dimension, respectively. Both olivines have compositions $Fo_{83}$; the euhedral crystals are rimmed by enstatite ($En_{87}$ $Wo_1$). In the more basic BFR-12 chondrule, olivine is more abundant in the form of 30 $\mu$m euhedral crystals. These olivines lay diagonally with respect to pyroxene elongation, and are directly zoned ($Fo_{81-74}$; Fig. 2c). Olivine inclusions ($Fo_{82}$) within the enstatite nuclei suggest earlier nucleation of olivine, followed by impact-favored nucleation of pyroxenes. Suggestion for the impact origin of pyroxenes is the side concavity in the pseudo-spherical shape of the BFR-12 chondrule (Fig. 1).

Enstatite is zoned from $En_{86}Wo_1$ to $En_{78}Wo_1$ and mantled by thin pigeonite rims ranging from $En_{76}Wo_6$ to $En_{75}Wo_{10}$

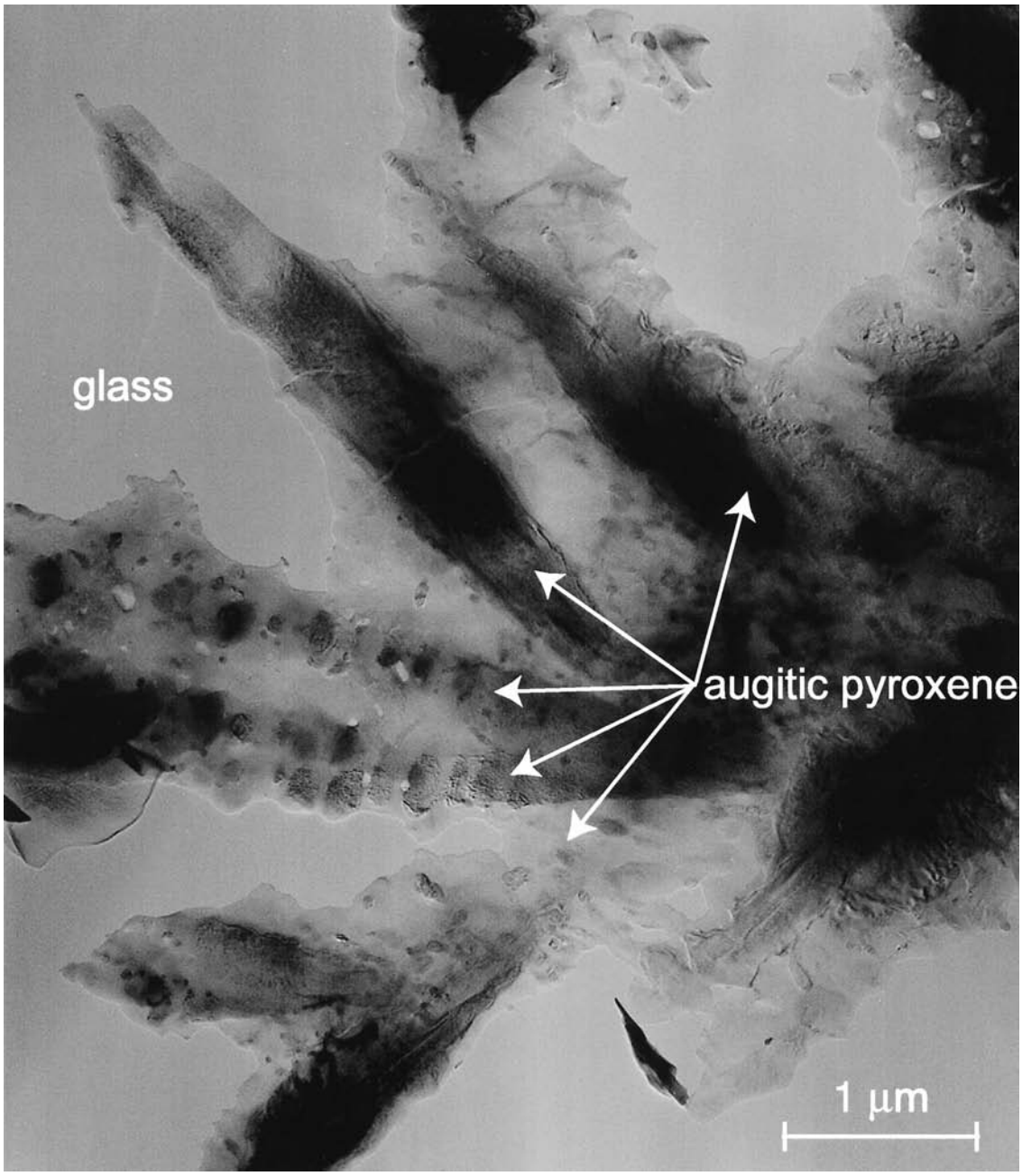


FIG. 5. Skeletal augitic pyroxene needles within the glass of POP chondrules.

(Fig. 2c). The enstatites are characterized by [100] stacking disorder, with orthoenstatite content increasing from 9 to 19% proceeding towards the rim. Unlike IIAB chondrules, no exsolution occurs in pigeonite of C IIB chondrules.

Augite is present both in FR3-3 and FR3-5 as euhedral grains within the glass (Fig. 2c), 1–2 $\mu$m in size with compositions $En_{52}Wo_{40}$ and $En_{58}Wo_{37}$, respectively.

The C IIB glass composition, unlike that in C IIAB chondrules, is homogeneous within the individual chondrules but varies from chondrule to chondrule (Fig. 2c). All the chondrules have very low K contents (the maximum value is ~10 atom% in FR3-5 chondrule), and different Na/(Na + Ca + Al) ratios. FR3-3 is the Na-richest glass, BFR-12 is (Ca + Al)-rich. Cr-rich spinel occurs within the C IIB glass.

The BFR-12 glass also hosts a Cr-rich spinel.

**Radial Pyroxene IIB**–RP chondrules (BFR-14 and FR32-2) are the smallest ones, with mean size of 280 $\mu$m (Fig. 1). They have the highest $SiO_2$ content and the lowest FeO, $Cr_2O_3$,

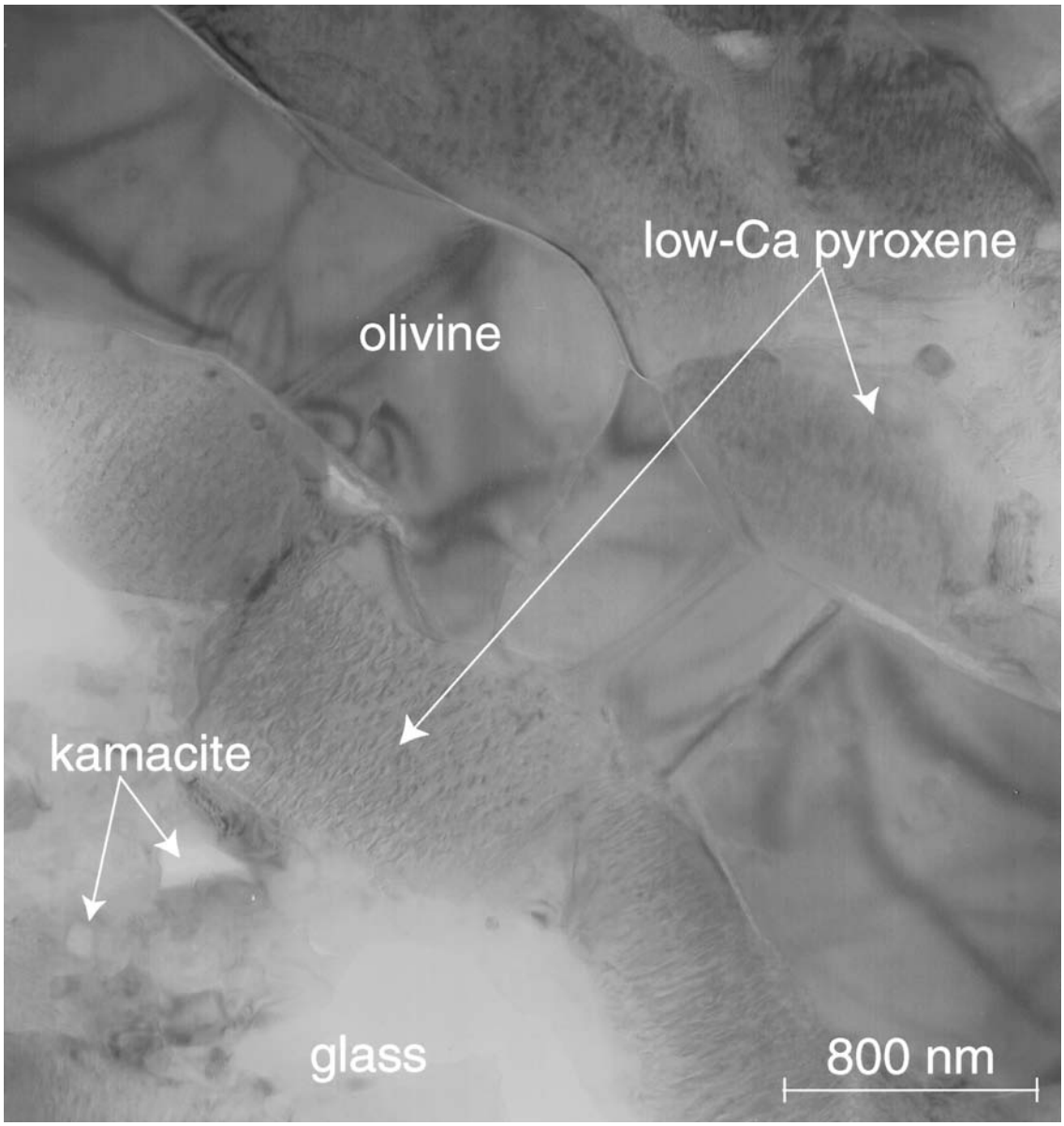


FIG. 6. TEM image of olivine, low-Ca pyroxene and kamacite within C-IIAB chondrules.

$Al_2O_3$, and $Na_2O$ content (Table 2), and have the lowest FeO/MgO ratio.

The two chondrules contain rare euhedral olivine grains, 2 to 10 $\mu$m in size. Two different igneous olivines are present in BFR-14: the first one, $Fo_{84}$, is included within enstatite cores; the second one, $Fo_{80}$, occurs within the glass (Fig. 2d). FR32-2 olivines are slightly zoned, from $Fo_{85}$ cores to $Fo_{81}$ rims.

The enstatite grains, 50–100 $\mu$m in size, $En_{76}Wo_3$ and $En_{94}Wo_1$ for BFR-14 and FR32-2, respectively, are remarkably zoned and surrounded by pigeonitic rims ($En_{70}Wo_{10}$ in BFR-14 and $En_{78}Wo_6$ in FR32-2; Fig. 2d).

Enstatite cores form 90% of the total crystal volume; [100] stacking disorder is maximal, with 31 and 42% orthoenstatite in their inner and outer zones, respectively. As in IIAB pyroxenes, the RP enstatites also have exsolved pigeonite or augite (FR32-2) external rims. In BFR-14, the pre-exsolution AEM rim composition is $En_{67}Wo_{17}$; the exsolution texture consists of $En_{73}Wo_5$ clinoenstatite hosting exsolved $En_{53}Wo_{31}$ sigmoids (Fig. 2d). Conversely, in FR32-2, the pre-exsolution rim composition is $En_{65}Wo_{32}$, and the exsolution texture consists of enstatite ($En_{93}$) sigmoids in $En_{53}Wo_{44}$ augite host. Actually, HRTEM images (Fig. 8) show sharp contact between the enstatite core and the exsolved pigeonitic rim; within the rim, a 4.5 Å matrix hosts exsolved sigmoids with $a$ periodicity of 9 Å. The $\lambda$ distances are 21 and 35 nm in BFR-14 and FR32-2, respectively, while $\sigma$ is ~12 nm for both samples.

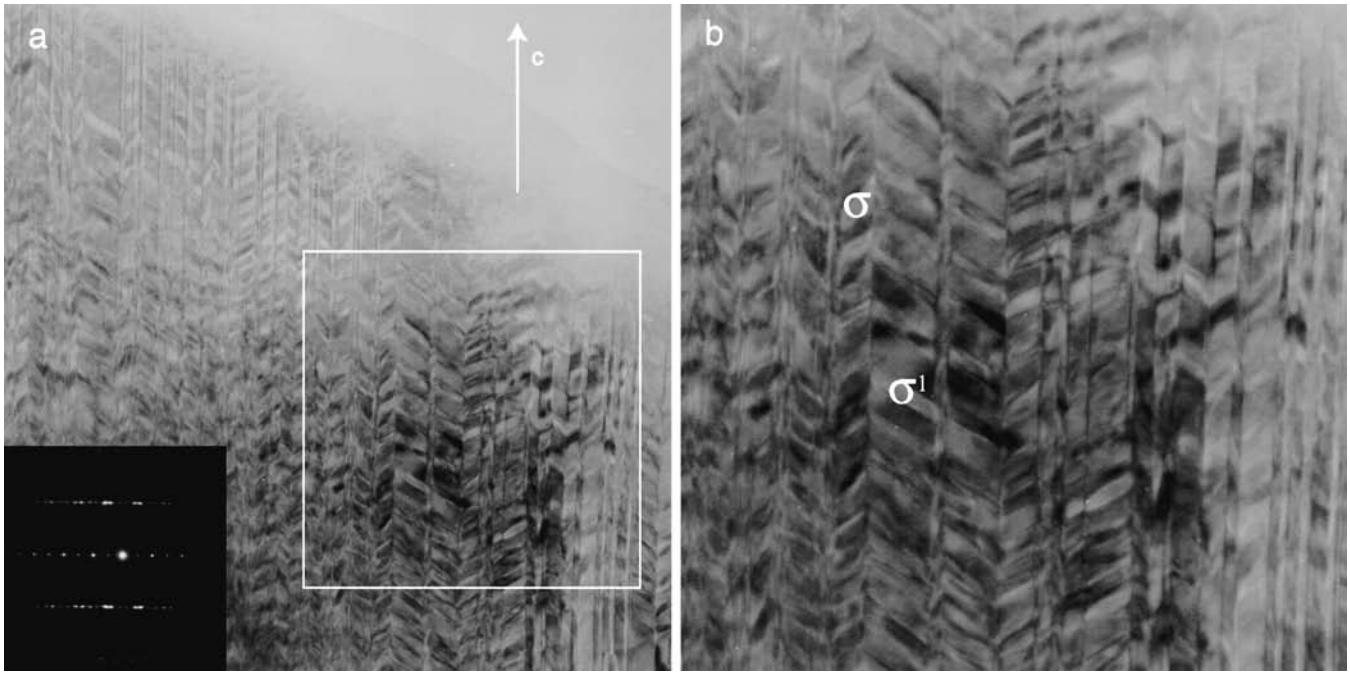


FIG. 7. TEM image of the exsolved external rim showing a complex twinned texture. (100) Microsynthetic twins formed through high-pigeonite to low-pigeonite phase transition, producing the vertical bands. Augite sigmoids ($\sigma$ and $\sigma^1$) occur in twin related orientation across the twin plane.

Glass is different in the two chondrules (Fig. 2d). BFR-14 glass occurs in two different textural settings; it is Al-enriched and alkalies-depleted when present as micrometric pockets between pyroxene crystals; it is alkalies-enriched when present as intergranular submicrometric thin films. FR32-2 glass occurs around pyroxene crystals as micrometric elongated pockets; it is homogeneous and extremely Al-enriched. Kamacite (3.3 wt% Ni) occurs within the BFR-14 glass.

**Barred Pyroxene IIB**–The FR3-4 chondrule is coarse grained, 970 $\mu$m in size (Fig. 1) and chemically resembles C IIB chondrules, although slightly FeO-depleted (Table 2). There is no evidence for olivine. Enstatite grains are elongated, with skeletal, dendritic habit; crystals are mutually separated by intermixed glassy layers 0.5 to 10 $\mu$m in thickness. Kamacite and Cr-rich spinel are included within enstatite. Enstatite is always mantled by pigeonite rims; their compositions are $En_{85}Wo_1$ and $En_{77}Wo_9$, respectively (Fig. 2e). Orthoenstatite lamellae are homogeneously distributed within clinoenstatite and sum up to 7% of the total volume.

Towards the most external part, the pigeonitic rim is exsolved. The pre-exsolution mean composition is $En_{66}Wo_{17}$; the post-exsolution matrix has composition of $En_{73}Wo_{11}$ and hosts sigmoidal domains of $En_{52}Wo_{41}$ composition (Fig. 2e). Mean width of the sigmoids ($\sigma$) is ~70 nm, while the distance between adjacent sigmoids ($\lambda$) is 102 nm.

Augite crystals occur within the glass. They are ~2 $\mu$m in size, euhedral, and with constant $En_{52}Wo_{44}$ compositions (Fig. 2e).

The glass has Si and Al contents between 62–82 and 10–18 atom%. Compositions are variable, with Na increasing and Al and Ca decreasing towards pyroxene crystal boundaries (Fig. 2e). Kamacite (4% Ni) and troilite occur within the two glasses, together with Na-rich feldspar ($Ab_{88}An_6Or_6$).

**Calcium-Aluminum-Rich Chondrule**–The BFR-7 chondrule, 230 $\mu$m in apparent diameter, is round and has fine-grained texture (Fig. 1); grain size ranges from 25 to <1 $\mu$m.

Together with rare grains of olivine (10–15 vol%) and Mg-rich pyroxene (10 vol%), BFR-7 contains primarily Ca-Mg rich pyroxenes (50 vol%), and secondarily Ca-rich plagioclases (10 vol%), Si-Al-rich glass (15 vol%) and submicrometric grains of a Ca-Mg-rich silicate. Presumably, this Ca-Mg-rich silicate is a wollastonite-like pyroxenoid but no crystallographic evidence was obtained because of its very small size; the chemical composition expressed as atom% is Si = 24.4 (1), Al = 0.3 (0.6), Cr = 0.3 (0.4), Ti = 1.9 (0.5), Mg = 6.3 (1.5), Fe = 2.7 (2.2), Ca = 21.0 (0.5) and O = 43. 5 (0.6) (mean squared deviation in parentheses).

The olivine, 25 $\mu$m in size, is euhedral, normally zoned ($Fo_{87-83}$; Fig. 2f), and contains glass inclusions.

Two different generations of enstatite grains are present; coarse-grained, relic-like crystals, 20 $\mu$m in size, with rounded grain boundaries, and 10 $\mu$m sized acicular crystals.

The relic-like pyroxene is zoned as the enstatite grains in type II chondrules. The enstatite ($En_{90}Wo_3$) is surrounded by pigeonitic rim ($En_{86}Wo_8$), as well as by an exsolved external

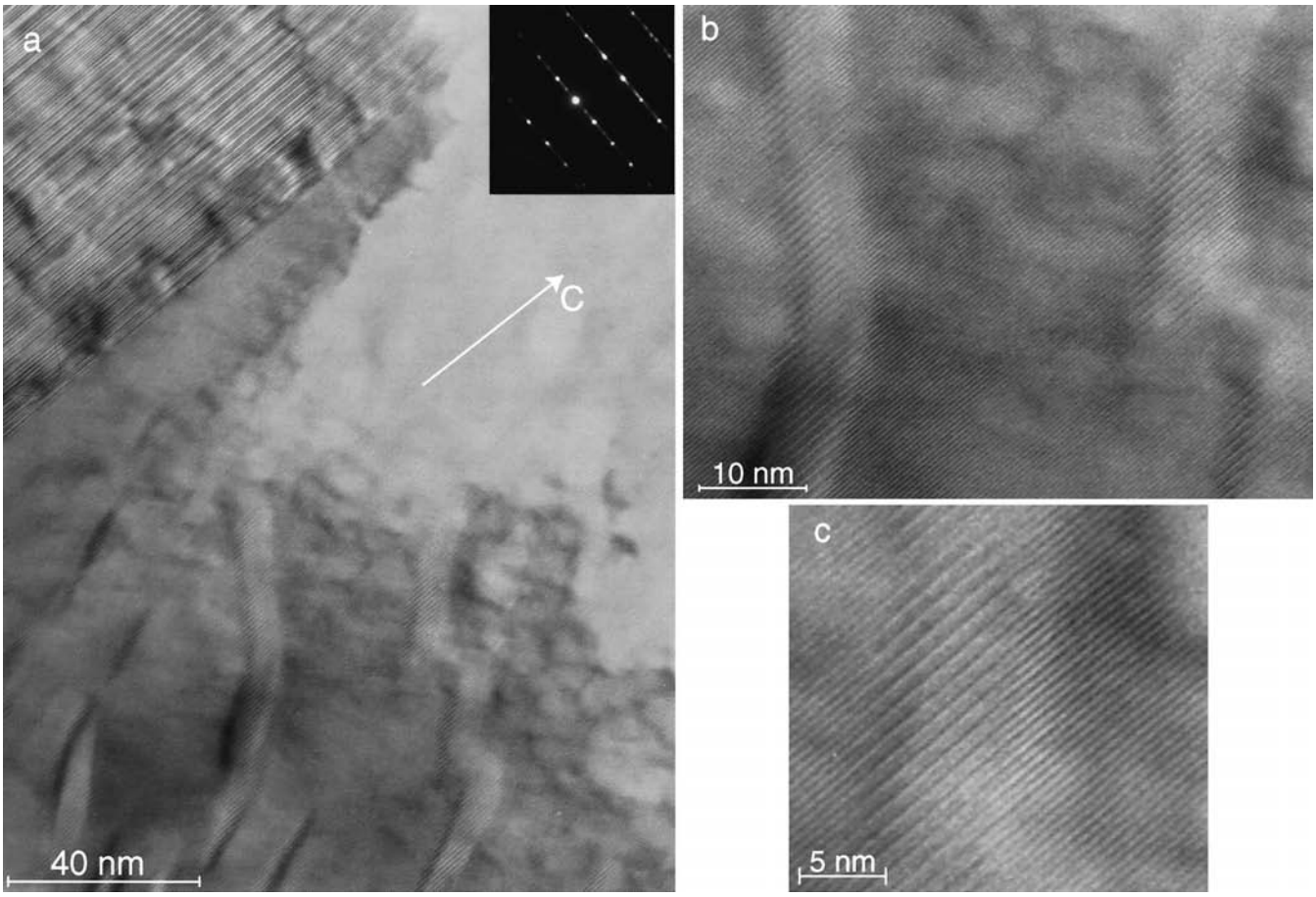


FIG. 8. (a) Sharp contact between the low-Ca core (top left), consisting of disordered orthoenstatite–clinoenstatite association, and the Ca-enriched, sigmoidally exsolved, pigeonitic rim in RP-IIB chondrules; (b) and (c) are enlarged views of the exsolution textures.

rim with mean composition $En_{57}Wo_{36}$ (Fig. 2f). The exsolution texture now consists of clinoenstatite sigmoids ($En_{87}Wo_5$) within augite host ($En_{58}Wo_{42}$), thus recalling FR32-2. The exsolved sigmoids are 13 nm wide ($\sigma$), with pseudoperiodic spacing ($\lambda$) of 19 nm. HRTEM images show that proceeding towards the pigeonitic rim the amount of orthoenstatite intergrown with clinoenstatite increases from 9 to 40%.

About 50% of the chondrule consists of zoned acicular pyroxenes with enstatitic cores ($En_{80}Wo_2$) surrounded by pigeonitic rim ($En_{82}Wo_8$) (Fig. 2f). Enstatite consists of intergrown orthoenstatite-clinoenstatite; orthoenstatite content increases from 12 to 21 vol% proceeding towards the pigeonitic rim. Also in this case, pigeonite is exsolved with augitic precipitates ($En_{61}Wo_{39}$) in a clinoenstatite host ($En_{84}Wo_5$), but exsolution produces here [001] lamellar-like domains ($\sigma = 10$ nm; $\lambda = 21$ nm) rather than sigmoids.

Glass hosts euhedral diopside grains ($En_{49}Wo_{44}$) smaller than 2 $\mu$m in size. Plagioclases are present in the glass as two different generations: (1) acicular, directly zoned labradorite ($An_{70-54}$) grains, 25 $\mu$m long and 1–2 $\mu$m wide, sometimes in sharp contact with Ca-rich pyroxene rims, and (2) very fine-grained 20–100 nm sized xenomorphic grains of anorthite. Rare submicrometric grains of putative Mg-rich wollastonite are present within the glass.

The glass is present in two different textural settings; when present as nanometer-sized inclusions within pyroxenes and/or olivines, it shows enrichments of $Na_2O$ and $K_2O$ (up to 9 and 1 wt%, respectively); when the glass occupies interstitial spaces between anorthite grains, alkalies are absent.

## Thermometric Constraints by Analytical Electron Microscopic Data

The accretion of chondrules (Wasson, 1993; Hewins, 1996) has been matter of debate, with alternative proposals that suggest either hot accretion (*e.g.*, Hutchison *et al.*, 1980) or cold accretion (*e.g.*, Haack *et al.*, 1992; Brearley and Jones, 1993). Therefore, any quantitative constraint able to limit crystallization from the melt, subsolidus evolution, or time-temperature-transformation (TTT) paths for as many of mineral

phases or mineral transformations as possible, may contribute to prove or disprove the different models.

Ca-Fe-Mg partitioning between coexisting pyroxenes is temperature dependent, and constitutes the basis for several two-pyroxene geothermometers (*e.g.*, Lindsley, 1983). However, the present textural analysis of chondrules from unequilibrated (or type 3) OC reveals that (1) phase relationships within pyroxenes may be complex; (2) electron microprobe data may not be sufficiently resolved; (3) pyroxenes are not necessarily in mutual equilibrium. Therefore, we used AEM compositions as input to the two-pyroxene thermometer. Estimates refer to crystallization temperatures only when textural equilibrium was reasonably approached, as for the exsolved textures in low-Ca pyroxene rims. Otherwise, our estimates provide the minimal crystallization temperature. All the estimates were obtained through the QUILF computer program, version 6.42 (Andersen *et al.*, 1993). Estimates of the exsolution temperatures were obtained by imposing equilibrated augite and pigeonite compositions. These temperatures may result 100 °C lower than estimates based upon the pigeonite ⇒ augite + orthopyroxene calibrated by Sack and Ghiorso (1994).

The crystallization temperature of olivine was estimated applying the geothermometer proposed by Leeman and Scheidegger (1977). Namely, we assumed that the measured mean chemical compositions of chondrules represent the groundmass chemical composition in equilibrium with the first crystallizing olivine grain (*i.e.*, the olivine cores).

Assuming igneous origin, maximal crystallization temperatures of plagioclase were estimated from their compositions, using the binary phase diagrams first proposed by Bowen (1913). On the other hand, minimal crystallization temperatures of alkali-feldspars were estimated using the ternary phase diagram by Seck (1971). However, we have no data to exclude a later metamorphic origin of feldspars present within the glass mesostasis.

**Porphyritic–Olivine Pyroxene IIAB**–In the different chondrules, the calculated crystallization temperatures for olivine are between 1506 and 1423 °C (Table 3).

Enstatite records minimal crystallization temperatures comprised between 1216 and 1295 °C. Coherently, the pigeonitic rim records lower values, ranging between 1239 and 1023 °C. The exsolved pigeonitic rims have compositions corresponding to minimal crystallization temperatures of 1031 and 1017 °C, respectively; exsolution occurs at 758 ± 65 °C and 640 ± 91 °C in BFR-8 and BFR-18, respectively.

In the case of high-Ca pyroxenes, a minimal crystallization temperature was estimated as 1066 and 1000 °C for BFR-18 and BFR-16, respectively. Skeletal pyroxenes crystallized above 1173 and 1068 °C.

Feldspars are present within the glass, in all chondrules except BFR-18. In the case of alkali-feldspars, minimal crystallization temperatures would be 750 °C. In the case of BFR-16 plagioclase, the maximal temperature would be close to 1280 °C.

**Cryptocrystalline IIAB**–Olivine crystallizes at temperatures between 1474 and 1454 °C.

The enstatite crystallization occurred at minimal temperatures between 1319 and 1258 °C, and the surrounding pigeonite rim between 1050 and 967 °C.

The mean AEM analyses of the exsolved external rim give minimal crystallization temperatures between 1025 and 983 °C. Exsolution occurred between 914 ± 88 °C and 856 ± 99 °C. The latter temperature matches our previous textural observations, when we suggested that the exsolved domains are subsequent to the (100) twin structure, expected to occur between 935 and 845 °C (Schröpfer, 1985).

FR3-1 and FR3-2 glasses embed feldspars yielding minimal crystallization temperatures of 750–800 °C and 600–650 °C for FR3-1 and FR3-2, respectively.

**Cryptocrystalline IIB**–Olivine crystallizes between 1459 and 1402 °C.

Minimal crystallization temperatures for enstatite cores are in between 1344 and 1242 °C, and pigeonitic rims in between 1179 and 1029 °C.

Augites within glass indicate minimal crystallization temperatures of 1072 and 1187 °C for FR3-3 and FR3-5, respectively.

Minimal crystallization temperature of 650 °C is obtained for the feldspars in the FR3-5 glass.

**Radial Pyroxene IIB**–Olivine crystallizes between 1414 and 1400 °C.

The enstatite cores indicate minimal crystallization temperature of 1366 and 1202 °C for BFR-14 and FR32-2, respectively; temperatures are 1009 and 1133 °C for the pigeonitic rims. Minimal temperatures of 1074 and 1191 °C were calculated for the outermost exsolved rims, with exsolution temperatures of 1018 ± 81 °C and 970 ± 32 °C.

Augite in FR32-2 records minimal crystallization temperature of 1006 °C.

**Barred Pyroxene IIB**–As there is no evidence of olivine, the earliest thermal estimate refers to enstatite, with minimal crystallization temperature of 1262 °C. The surrounding pigeonite rim indicates a temperature of 1050 °C. The outermost pigeonite rim, crystallized at 1069 °C, exsolved at 890 ± 127 °C.

Ca-rich pyroxene in the glass gives a minimal temperature of 957 °C.

**Calcium-Aluminum-Rich Chondrule**–The olivine grain indicates crystallization temperatures of 1400 °C (Table 4). The enstatite core records minimal crystallization temperature of 1182 °C and the pigeonitic rim of 1091 °C. Proceeding towards the outermost, exsolved rim the mean composition indicates a temperature of 1192 °C. Finally the exsolution temperature is 834 ± 64 °C.

The other zoned low-Ca pyroxenes record minimal crystallization temperature of 1295 °C, with pigeonitic rim pointing to 1066 °C. The mean chemical composition of the exsolved pigeonitic rim gives minimal temperature of 1268 °C, and exsolution temperature of 1067 ± 65 °C.

The plagioclase with labradoritic compositions ($An_{70-54}$) gives maximal crystallization temperatures between 1400 and 1280 °C. Pure anorthite indicates maximal temperature of crystallization close to 1550 °C.

### Speedometric Constraints

Many experiments were designed to constrain cooling rates of chondrules. For instance, values ranging from 5 °C/h to some thousands degrees Celsius per hour were obtained based upon crystal shapes and Fe/Mg zoning in olivine (Hewins, 1983, 1988; Jones and Lofgren, 1993; Lofgren, 1996; Weinbruch *et al.*, 2001).

Further constraints may be inferred from enstatite microstructures, as proto-enstatite inverts to twinned clinoenstatite upon quenching, to orthoenstatite upon slow cooling, to disordered orthoenstatite/clinoenstatite intergrowth upon intermediate cooling rate (Buseck *et al.*, 1980). In particular, Brearley and Jones (1993) calibrated the orthoenstatite/clinoenstatite speedometer for fixed compositions ($En_{100}$ and $En_{84}Wo_1$). As our pyroxenes may have slightly different compositions ($En_{94-70}$), the use of the Brearley and Jones speedometer here is partially uncalibrated. The cooling rates so estimated are reported in Table 5 and refer to the proto-enstatite inversion temperature of 1250–1200 °C. In particular:

- In POP chondrules, the presence of 5% orthoenstatite lamellae at the crystal cores indicates fast cooling rates, in the order of thousands degrees per hour (5000 °C/h). Moving towards the pigeonitic rim, the estimated cooling rate decreases to ~1000 °C/h.
- The BP chondrule FR3-4 indicates a very fast cooling rate (3500 °C/h).
- Both the C IIAB and C IIB enstatite cores indicate cooling rates of about 1000–3000 °C/h.
- Slower cooling rates are recorded by RP chondrules. In fact, cooling rates are about 100 and 50 °C/h at crystal core and periphery, respectively.
- The Ca-Al-rich chondrule (BFR-7) indicates cooling rates of 3000 to 60 °C/h and 2500 to 700 °C/h, for relic and second-generation enstatite, respectively.

## DISCUSSION

### Crystallization Sequence

The previous data lead us to formulate the following crystallization sequence for type II chondrules. This crystallization sequence is completely general, and outlines the most important textural evidence.

**Olivine**–Olivine is the earliest phase nucleating from the melt. Olivines exhibit different habits (*e.g.*, euhedral or skeletal), possibly related to both different cooling rates, as well as to the presence of previous solid nuclei capable of favoring olivine nucleation.

**Proto-Enstatite**–Proto-enstatite crystallizes after olivine. During subsolidus evolution, proto-enstatite transforms into twinned, disordered clinoenstatite by displacive phase transition.

**Pigeonitic**–Pigeonitic discontinuous rims (or, less frequently, *augitic* rims) surround the enstatite cores. By subsolidus evolution, high-pigeonite inverts to twinned low-pigeonite.

**Augite**–Augite crystallizes as euhedral grains hosted within the glassy matrix, or as skeletal crystals, most probably just fter the pigeonitic rim growth.

**Pigeonitic and Augitic Rims**–Pigeonitic and augitic rims exsolve forming augitic and enstatitic sigmoids, respectively.

As we never observed "U-shaped" or "Z-shaped" terminations (present in the La Villa H4 enstatite and explained

TABLE 5. Orthoenstatite/clinoenstatite in enstatite cores and $\lambda$ and $\sigma$ values for exsolved textures in pigeonitic rims.

| | Enstatite core | | Exsolved pigeonitic rim | |
|---|---|---|---|---|
| | Orthoenstatite (vol%) in inner and outer core | Estimated cooling rates (°C/h) in the 1250–1200 °C range | $\lambda$ (nm)* | $\sigma$ (nm)* |
| POP | 5–15 | 5000–1100 | 36–37 | 13 |
| C IIAB | 14–21 | 1100–700 | 18 | 7–8 |
| C IIB | 9–19 | 3000–800 | – | – |
| RP | 31–42 | 200–60 | 21–35 | 12 |
| BP | 7–7 | 3500 | 102 | 70 |
| Ca-Al rich† | 9–40 | 3000–60 | 19 | 13 |
| Ca-Al rich‡ | 12–21 | 2500–700 | 21 | 10 |

*$\lambda$ is the average, pseudoperiodic spacing of the exsolution texture measured as the average distance along [001] between adjacent augite sigmoids. $\sigma$ is the mean width of sigmoids measured along the same direction that is ~13 nm.
†Relic enstatite.
‡"New" enstatite.
Abbreviations: POP = porphyritic–olivine pyroxene; C = cryptocrystalline; BP = barred pyroxene; RP = radial pyroxene.

in terms of accretional annealing; Folco and Mellini, 2000), we confirm the primitive nature of the present meteorites.

## The Analytical Electron Microscopic Chondrule Geothermometry

Different groups of type II chondrules share common main mineral features that correspond to common main thermal events (Table 6). Therefore, in agreement with textural observations (see "Crystallization Sequence"), we conclude that:

- Olivine formed between 1500 and 1400 °C.
- Proto-enstatite crystallized at temperatures of 1350–1200 °C. The proto-enstatite compositions are consistent with proto-enstatite → clinoenstatite inversion at temperatures of 1200–1250 °C (Huebner and Turnock, 1980).
- Pigeonitic rims formed at $T > 1000$ °C. By subsolidus evolution, high-pigeonite inverted to low-pigeonite between 935 and 845 °C.
- Augites crystallized between 1150 and 1000 °C.
- Pigeonitic and augitic rims, by subsolidus evolution, exsolved between 1000 and 640 °C.
- Based upon *glass* composition, we infer that the overall solidification temperature was close to 990 °C, which is the appropriate minimum melt in the quartz–albite–orthoclase system (Hamilton and Mackenzie, 1965).

## Cooling Rates

Coarse-grained POP chondrules have faster orthoenstatite/clinoenstatite cooling rates than finer grained radial RP chondrules. This feature may be explained based upon the experimental data by Lofgren (1996). These experiments show that final textures depend either on cooling rate from the melt state, or on the occurrence of unmelted inclusions. These inclusions induce crystal growth and allow the development of porphyritic textures even under high cooling rate. By contrast, radial chondrules result from crystallization of completely melted chondrules, in absence of nucleation seeds. Similar cooling rates (100 °C/h) were found in a RP chondrule from the H4 La Villa chondrite (Folco and Mellini, 2000).

One more insight on cooling rate may be inferred from exsolution microstructures (Weinbruch *et al.*, 2001; Müller *et al.*, 1995; Weinbruch and Müller, 1995; Watanabe *et al.*, 1985; Kitamura *et al.*, 1983; Carpenter, 1978). In particular, "lamellar" exsolution models have been proposed by Weinbruch and Müller (1995). These authors describe, in GOP Allende chondrules, the presence of pigeonite/diopside exsolution lamellae, produced under cooling rates of 25–7 °C/h, from 1350 to 1200 °C. For synthetic analogues of chondrules, Weinbruch *et al.* (2001) report [001] coherent exsolution pigeonite/augite lamellae produced under cooling rates of 50–10 °C/h, from 1455 to 1000 °C; higher cooling rates (450–50 °C/h) yield only modulated structures with a wavelength on the order of 17–19 nm for the [001] orientation. In natural chondrules, however, we found sigmoidal precipitates rather than lamellar associations. At present, we do not yet know the exact meaning of sigmoids with respect to lamellae. Therefore we envisage to further study structure and origin of sigmoids.

As far as we know, this is the first time that sigmoidal arrangements are systematically observed in chondrites. Previously, sigmoids were found in the H4 Raguli chondrite (Folco, 1997). Similar but coarser structures may be found in the Moore County eucrite (Fig. 3 in Takeda *et al.*, 1981). Similar structures have also been noted in synthetic pigeonite by Feuer *et al.* (1989) and named "S-shaped precipitates". According to Feuer *et al.* (1989), S-shaped precipitates formed under cooling rate of 8 °C/h, from 1350 °C to room temperature. As our exsolution texture show $\sigma$ thickness (Table 5) and compositions similar to those described by Feuer *et al.* (1989), we infer similar cooling rates. In particular, however, our sigmoids may be thicker than those observed by Feuer *et al.* (1989). Therefore, assuming a reasonable (yet undemonstrated) relationship

TABLE 6. Summary of crystallization temperatures for the different chondrule types.

| | Range of crystallization $T$ (°C) for olivine | Range of minimal crystallization $T$ (°C) for enstatite core | Range of minimal crystallization $T$ (°C) for pigeonite rim | Range of minimal crystallization $T$ (°C) for exsolved rim (pre-exsolution) | Range of exsolution $T$ (°C) for exsolved structure | Range of minimal crystallization $T$ (°C) for high-Ca pyroxene |
|---|---|---|---|---|---|---|
| POP-IIAB | 1423–1506 | 1216–1295 | 1023–1239 | 1017–1031 | 640 ± 91 – 758 ± 65 | 1066–1160 |
| C-IIAB | 1445–1474 | 1258–1319 | 967–1050 | 983–1025 | 856 ± 99 – 914 ± 88 | – |
| C-IIB | 1402–1459 | 1242–1344 | 1029–1179 | – | – | 1072–1187 |
| BP-IIB | – | 1262 | 1050 | 1069 | 890 ± 127 | 957 |
| RP-IIB | 1400–1414 | 1202–1366 | 1009–1133 | 1074–1191 | 970 ± 32 – 1018 ± 81 | 1006 |
| Ca-Al rich | 1400 | 1182–1295 | 1066 | 1192–1268 | 964–1067 | – |
| Ranges | 1400–1500 | 1200–1350 | 1000–1250 | 1000–1250 | 650–1050 | 950–1200 |

Abbreviations: POP = porphyritic–olivine pyroxene; C = cryptocrystalline; BP = barred pyroxene; RP = radial pyroxene.

between $\sigma$ and cooling rate, we suggest that the chondrules studied in the present work cooled at different rates <8 °C/h in the 1000–640 °C exsolution temperature range.

The different features (olivine zoning, orthoenstatite/clinoenstatite disorder, precipitates) reflect the nonlinear, decreasing cooling rate of chondrites. At higher temperature (olivine crystallization or proto-enstatite inversion), chondrule cooling rates typically are in the order of thousands to hundreds degrees Celsius per hour. At subsolidus temperature (pigeonite exsolution), cooling rates are 2–3 orders of magnitudes lower (several degrees Celsius per hour or slower). Still slower cooling rates occur at lower temperatures. For instance, based upon Fe-Mg ordering in enstatite from H-, L- and LL-ordinary chondrites, Folco *et al.* (1997) found cooling rates ranging from a few degrees Celsius per thousand years to 100 °C/ka in the 340–480 °C interval.

One more conclusion regards the environment where chondrules cooled. The different orthoenstatite/clinoenstatite and exsolution cooling rates, recorded by texturally distinct chondrules from the same meteorite, indicate thermal histories established prior to accretion into the parent body, within physico-chemically different environments. In particular, as the lowest recorded exsolution temperature is 640 ± 91 °C (BFR-18; Table 3), the accretion of chondrules into the parent body would have occurred at still lower temperature.

## CONCLUSIONS

The TEM-AEM study of type II (FeO-rich) chondrules, different in textures, from H3.4–H3.6 chondrites (Brownfield; FRO 90003; FRO 90032) better defines the crystallization history and subsolidus evolution of primitive H chondrites. Furthermore, the nanotextural and nanochemical data help to constrain their formation environment. In particular, we conclude that:

- The crystallization sequence (olivine; proto-enstatite; pigeonitic rim; augite) is similar in all the analyzed chondrules. However, (1) the bulk composition, (2) the presence/absence of grains capable of acting as nucleation seeds, and (3) the different cooling rates, all these features contribute to originate the different chondrule macrotextures.
- On cooling, proto-enstatite inverts to clinoenstatite and orthoenstatite between 1250 and 1000 °C. Estimated cooling rates are on the order of 50–3000 °C/h.
- Pigeonite transforms from high- to low-pigeonite, close to 935–845 °C.
- The pigeonitic rims exsolve producing sigmoidal precipitates, indicating variable cooling rates of <8 °C/h in the 1000–640 °C range.
- Sigmoidal precipitates are common in primitive ordinary chondrites. Possibly, future calibration of the growth of sigmoids may help in further constraining cooling rates.
- The chondrule cooling path is definitely nonlinear; faster in the range of the proto-enstatite inversion, it decreases at the pyroxene exsolution.
- Our observations are in keeping with a scenario where chondrules formed within separate environments, by multiple flash heating. The temperature of chondrule accretion into the parent planetesimal was lower than 650 °C.
- TEM and AEM techniques are very powerful investigation methods, capable of revealing important thermal markers in meteorites. A possible follow-up of this study is the systematic investigation of nanostructural and nanochemical evolution with the increasing petrographic type (*e.g.*, in H4 to H5 OC).

*Acknowledgements*–We thank J. I. Goldstein, R. H. Hewins, G. E. Lofgren, S. Weinbruch for their constructive and helpful reviews of an earlier version of this manuscript.

*Editorial handling*: J. I. Goldstein

## REFERENCES

ANDERSEN D. J., LINDSLEY D. H. AND DAVIDSON P. M. (1993) QUILF: A Pascal program to assess equilibria among Fe-Mg-Mn-Ti oxides, pyroxenes, olivines, and quartz. *Comp. Geosci.* **19**, 1333–1350.

ASHWORTH J. R. (1980) Chondrite thermal histories: Clues from electron microscopy of orthopyroxene. *Earth Planet. Sci. Lett.* **46**, 167–177.

ASHWORTH J. R. (1981) Fine structure in H-group chondrites. *Proc. Royal Soc. London* **A374**, 179–194.

BOWEN N. L. (1913) Equilibrium diagram of the plagioclase feldspars. *Am. J. Sci.* **35**, 557–599.

BREARLEY A. J. AND JONES R. H. (1993) Chondrite thermal histories from low-Ca pyroxene microstructure: Autometamorphism *vs.* prograde metamorphism rivisited (abstract). *Lunar Planet. Sci.* **24**, 185–186.

BRIZI E. AND MELLINI M. (1992) Kinetical modelling of exsolution textures in igneous pyroxenes. *Acta Vulcanologica* **2**, 87–93.

BUSECK P. R., NORD G. L. AND VEBLEN D. R. (1980) Subsolidus phenomena in pyroxenes. In *Pyroxenes* (ed. C. T. Prewitt), pp. 117–211. Mineral. Soc. Am., Washington, D.C., USA.

CARPENTER M. A. (1978) Nucleation of augite at antiphase boundaries in pigeonite. *Phys. Chem. Mineral.* **2**, 237–251.

CARPENTER M. A. (1979) Experimental coarsening of antiphase domains in a silicate mineral. *Science* **206**, 681–683.

CONNOLLY H. C. AND HEWINS R. H. (1991) The influence of bulk composition and dynamic melting conditions on olivine chondrule textures. *Geochim. Cosmochim. Acta* **55**, 2943–2950.

DODD R. T. (1981) *Meteorites: A Petrologic–Chemical Synthesis.* Cambridge Univ. Press, Cambridge, U.K. 368 pp.

DUNCUMB P. AND REED S. J. B. (1968) The calculation of stopping power and backscattered effects in electron probe analysis. In *Quantitative Electron Probe Microanalysis* (ed. K. F. J. Heinrich), pp. 133–154. NBS Special Publication **298**, Government Printing Office, Washington, D.C., USA.

FEUER H., SCHRÖPFER L., FUESS H. AND JEFFERSON D. A. (1989) High resolution transmission electron microscopy study of exsolution in synthetic pigeonite. *Eur. J. Mineral.* **1**, 507–516.

FOLCO L. (1997) Pyroxene thermometry in chondritic meteorites. Ph.D. dissertation, The Open University, Milton Keynes, U.K. 188 pp.

FOLCO L. AND MELLINI M. (2000) Enstatite chemical composition and microstructures in the La Villa H4 chondrite. *Meteorit. Planet. Sci.* **35**, 733–742.

FOLCO L. AND RASTELLI N. (2000) The meteorite collection of the Museo nazionale dell'Antartide in Siena. *Meteorit. Planet. Sci.* **35 (Suppl.)**, A189–A198.

FOLCO L., MELLINI M. AND PILLINGER C. T. (1997) Equilibrated ordinary chondrites: Constraints for thermal history from iron-magnesium ordering in orthopyroxene. *Meteorit. Planet. Sci.* **32**, 567–575.

GOODING J. L. AND KEIL K. (1981) Relative abundances of chondrule primary textural types in ordinary chondrites and their bearing on conditions of chondrules formation. *Meteoritics* **16**, 17–43.

GROSSMAN J. N. (1988) Formation of chondrules. In *Meteorites and the Early Solar System* (eds. J. F. Kerridge and M. S. Matthews), pp. 660–679. Univ. Arizona Press, Tucson, Arizona, USA.

GROSSMAN J. N., RUBIN A. E., NAGAHARA H. AND KING E. A. (1988) Properties of chondrules. In *Meteorites and the Early Solar System* (eds. J. F. Kerridge and M. S. Matthews), pp. 619–659. Univ. Arizona Press, Tucson, Arizona, USA.

HAACK H., TAYLOR G. J., SCOTT E. R. AND KEIL K. (1992) Thermal history of chondrites: Hot accretion *vs.* metamorphic reheating. *Geophys. Res. Lett.* **19**, 2235–2238.

HAMILTON D. I.. AND MACKENZIE W. S. (1965) Phase equilibrium studies in the system $NaAlSiO_4$–$KAlSiO_4$–$SiO_2$–$H_2O$. *Mineral. Mag.* **34**, 214–231.

HEUER A. H. AND NORD G. L., JR. (1976) Polymorphic phase transitions in minerals. In *Electron Microscopy in Mineralogy* (ed. H. R. Wenk), pp. 274–303. Springer-Verlag, New York, New York, USA.

HEWINS R. H. (1983) Dynamic crystallization experiments as constraints on chondrule genesis. In *Chondrules and Their Origins* (ed. E. A. King), pp. 122–123. Lunar and Planetary Institute, Houston, Texas, USA.

HEWINS R. H. (1988) Experimental studies of chondrules. In *Meteorites and the Early Solar System* (eds. J. F. Kerridge and M. S. Matthews), pp. 660–679. Univ. Arizona Press, Tucson, Arizona, USA.

HEWINS R. H. (1997) Chondrules. *Ann. Rev. Earth Planet. Sci.* **25**, 61–83.

HEWINS R. H. AND CONNOLLY H. C. (1994) Experimental constraints on models for origins of chondrules: Peak temperatures (abstract). In *Chondrules and the Protoplanetary Disk* (eds. R. H. Hewins, R. H. Jones and E. R. D. Scott), pp. 11–12. LPI Contribution No. **844**, Lunar and Planetary Institute, Houston, Texas, USA.

HEWINS R. H., JONES R. H. AND SCOTT E. R. D., EDS. (1996) *Chondrules and the Protoplanetary Disk.* Cambridge Univ Press, Cambridge, U.K. 346 pp.

HUEBNER J. S. AND TURNOCK A. C. (1980) The melting relations at 1 bar of pyroxenes composed largely of Ca-, Mg-, and Fe-bearing components. *Am. Mineral.* **65**, 225–271.

HUTCHINSON R., BEVAN A. W. R., AGRELL S. O. AND ASHWORTH J. R. (1979) Accretion temperature of the Tieschitz, H3, chondritic meteorite. *Nature* **280**,116–119.

HUTCHINSON R., BEVAN A. W. R., AGRELL S. O. AND ASHWORTH J. R. (1980) Thermal history of the H-group chondritic meteorites. *Nature* **287**, 787–790.

IIJIMA S. AND BUSECK P. R. (1975) High resolution electron microscopy of enstatite. I: twinning, polymorphism, and polytypism. *Am. Mineral.* **60**, 758–770.

JONES R. H. (1994) Petrology of FeO-poor, porphyritic pyroxene chondrules in the Semarkona chondrite. *Geochim. Cosmochim. Acta* **58**, 5325–5340.

JONES R. H. AND LAYNE G. D. (1997) Minor and trace element partitioning between pyroxene and melt in rapidly cooled chondrules. *Am. Mineral.* **82**, 534–545.

JONES R. H. AND LOFGREN G. E. (1993) A comparison of FeO-rich, porphyritic olivine chondrules in unequilibrated chondrites and experimental analogues. *Meteoritics* **28**, 213–221.

KENNEDY A. K., LOFGREN G. E. AND WASSERBURG G. J. (1993) An experimental study of trace element partitioning between olivine, orthopyroxene and melt in chondrules: Equilibrium values and kinetic effects. *Earth Planet. Sci. Lett.* **115**, 177–195.

KERR R. A. (2001) A meteoriticist speaks out, his rocks remain mute. *Science* **293**, 1581–1584.

KITAMURA M., YASUDA M., WATANABE S. AND MORIMOTO N. (1983) Cooling history of pyroxene chondrules in the Yamato-74191 chondrite (L3)—An electron microscopic study. *Earth Planet. Sci. Lett.* **63**, 189–201.

LEEMAN W. P. AND SCHEIDEGGER K. F. (1977) Olivine/liquid distribution coefficients and a test for crystal-liquid equilibrium. *Earth Planet. Sci. Lett.* **35**, 247–257.

LINDSLEY D. H. (1983) Pyroxene thermometry. *Am. Mineral.* **68**, 477–493.

LOFGREN G. E. (1983) Effect of heterogeneous nucleation on basaltic textures: A dynamic crystallization study. *J. Petrol.* **24**, 229–255.

LOFGREN G. E. (1989) Dynamic crystallization of chondrule melts of porphyritic olivine composition: Textures experimental and natural. *Geochim. Cosmochim. Acta* **53**, 461–470.

LOFGREN G. E. (1996) A dynamic crystallization model for chondrule melts. In *Chondrules and the Protoplanetary Disk* (eds. R. H. Hewins, R. H. Jones and E. R. D. Scott), pp. 187–196. Cambridge Univ. Press, Cambridge, U.K.

LOFGREN G. E. AND LANIER A. B. (1990) Dynamic crystallization study of barred olivine chondrules. *Geochim. Cosmochim. Acta* **54**, 3537–3551.

LOFGREN G. E. AND RUSSELL W. J. (1986) Dynamic crystallization of chondrule melts of porphyritic and radial pyroxene composition. *Geochim. Cosmochim. Acta* **50**, 1715–1726.

MCSWEEN H. Y. (1977) Chemical and petrographic constraints on the origin of chondrules and inclusions in carbonaceous chondrites. *Geochim. Cosmochim. Acta* **41**, 1843–1860.

MORIMOTO N. (1989) Nomenclature of pyroxenes. *Can. Mineral.* **27**, 143–156.

MÜLLER W. F., WEINBRUCH S., WALTER R. AND MÜLLER-BENEKE G. (1995) Transmission electron microscopy of chondrule minerals in the Allende meteorite: Constraints on the thermal and deformational history of granular olivine-pyroxene chondrules. *Planet. Space Sci.* **43**, 469–483.

NEHRU C. E., WEISBERG M. K. AND PRINZ M. (1997) Chromites in unequilibrated ordinary chondrites (abstract). *Lunar Planet. Sci.* **28**, #1651, Lunar and Planetary Institute, Houston, Texas, USA (CD-ROM).

SACK R. O. AND GHIORSO M. S. (1994) Thermodynamics of multicomponent pyroxenes: II. Phase relations in the quadrilateral. *Contrib. Mineral. Petrol.* **116**, 287–300.

SCHRÖPFER L. (1985) Observation of reactions in synthetic Ca-poor pyroxene single crystals at elevated temperatures by x-ray diffraction. *Phys. Chem. Mineral.* **12**, 49–54.

SEARS D. W. G., GROSSMAN J. N., MELCHER C. L., ROSS L. M. AND MILLS A. A. (1980) Measuring metamorphic history of unequilibrated ordinary chondrites. *Nature* **287**, 791–795.

SECK H. A. (1971) Koexistierente alkali-feldspäte und plagioklase im system $NaAlSi_3O_8$-$KAl$ $Si_3O_8$-$CaAl_2$ $Si_2O_8$-$H_2O$ bei

temperaturen von 650 °C bis 900 °C. *Neues Jahrb. Mineral. Abh.* **115**, 315–395.

SCOTT E. R. D. AND TAYLOR G. J. (1983) Chondrules and other components in C, O, and E chondrites: Similarities in their properties and origins. *J. Geophys. Res.* **88**, B275–B286.

STÖFFLER D., KEIL K. AND SCOTT E. R. D. (1991) Shock metamorphism of chondrites. *Geochim. Cosmochim. Acta* **55**, 3845–3867.

TAKEDA H., MORI H., ISHII T. AND MIYAMOTO M. (1981) Thermal and impact histories of pyroxenes in lunar eucrite-like gabbros and eucrites. *Proc. Lunar Planet. Sci.* **12B**, 1297–1313.

TÖPEL-SCHADT J. AND MÜLLER W. F. (1985) The submicroscopic structure of the unequilibrated ordinary chondrites, Chainpur, Mezö-Madaras, and Tieschitz: A transmission electron microscope study. *Earth Planet. Sci. Lett.* **74**, 1–12.

TSUCHIYAMA A., NAGAHARA H. AND KUSHIRO I. (1980) Experimental reproduction of textures of chondrules. *Earth Planet. Sci. Lett.* **48**, 155–165.

VAN SCHMUS W. R. AND WOOD J. A. (1967) A chemical-petrologic classification for chondritic meteorites. *Geochim. Cosmochim. Acta* **31**, 747–765.

WASSON J. T. (1993) Constraints on chondrule origins. *Meteoritics* **28**, 14–28.

WATANABE S., KITAMURA M. AND MORIMOTO N. (1985) A transmission electron microscope study of pyroxene chondrules in equilibrated L-group chondrites. *Earth Planet. Sci. Lett.* **72**, 87–98.

WEINBRUCH S. AND MÜLLER W. F. (1995) Constraints on the cooling rates of chondrules from the microstructure of clinopyroxene and plagioclase. *Geochim. Cosmochim. Acta* **59**, 3221–3230.

WEINBRUCH S., MÜLLER W. F. AND HEWINS R. H. (2001) A transmission electron microscope study of exsolution and coarsening in iron-bearing clinopyroxene from synthetic analogues of chondrules. *Meteorit. Planet. Sci.* **36**, 1237–1248.

WLOTZKA F. (1993) A weathering scale for the ordinary chondrites (abstract). *Meteoritics* **28**, 640.